



The 24 January 2020 Mw 5.0 El Aouana Earthquake, Northeastern Algeria: Insights into a New NW–SE Right-Lateral Bejaia-Babors Shear Zone

ISSAM ABACHA,¹ OUALID BOULAHIA,¹ ABDELKARIM YELLES-CHAOUCHE,¹ HICHEM BENDJAMA,¹ HAAKON FOSSEN,² MOULLEY CHARAF CHABOU,³ KHALED ROUBECHÉ,¹ SOFIANE TAKI-EDDINE RAHMANI,¹ EL-MAHDI TIKHAMARINE,⁴ YAHIA MOHAMMEDI,¹ and CHAFIK AIDI¹

Abstract—On January 24, 2020, a Mw 5.0 earthquake occurred in the El Aouana region, northeastern Algeria. This region is located at the western end of the Lesser Kabylia Block (LKB), a rigid body that was weakly deformed during the late Cenozoic tectonic phase, and it is characterized by a lower seismic activity than that in its bounding regions. The mainshock focal mechanism was estimated via both the P-wave first motion and waveform modeling methods. The earthquake was associated with the rupture of a NW–SE-oriented right-lateral strike-slip fault, as revealed by a 6 km long and 2 km wide aftershock cluster. The seismic moment estimated through waveform modeling was 3.6×10^{16} Nm, while spectral analysis yielded a value of 3.9×10^{16} Nm corresponding to a magnitude of Mw 5.0, a source radius of 1.6 km, and a stress drop of 4 MPa. The spatiotemporal evolution of the aftershock sequence, as modeled using a restricted epidemic-type aftershock sequence (RETAS) stochastic model, yielded a slope $p = 1$, indicating that the earthquake was generated by tectonic forces and that the aftershock sequence included many subsequences. The calculated stress tensor suggested N–S compression, rotated clockwise relative to NW–SE Eurasia–Africa convergence. Finally, the recent seismic activity (2012–2021) and geological observations in the area led to the suggestion of a new NW–SE right-lateral shear zone, namely, the Bejaia-Babors shear zone, which was incorporated into a seismotectonic growth model involving slip along inherited E–W structures. The pattern of stepover structures throughout this wide shear zone was enhanced during the recent seismic evolution.

Keywords: El Aouana, RETAS, source parameters, stress tensor, shear zone, stepovers.

Supplementary Information The online version contains supplementary material available at <https://doi.org/10.1007/s00024-023-03265-3>.

¹ Center of Research in Astronomy, Astrophysics, and Geophysics, CRAAG, Route de l’Observatoire BP 63 Bouzaréah, Algiers, Algeria. E-mail: abacha.issam@yahoo.fr

² Museum of Natural History, University of Bergen, Allégaten 41, 5007 Bergen, Norway.

³ Emerging Materials Research Unit, Department of Earth Sciences, Institute of Architecture and Earth Sciences, Ferhat Abbas University Setif 1, Setif, Algeria.

⁴ Département de Physique, Ferhat Abbas University Setif 1, Setif, Algeria.

1. Introduction

Northeastern Algeria is subjected to substantial, moderate, and shallow seismic activity due to its location along the African–Eurasian plate boundary (blue line in Fig. 1a). One of the main statistical characteristics of Algerian seismicity is its concentration in the country’s eastern part, where nearly two-thirds of the recorded seismic events have occurred (Abacha, 2015; Yelles-Chaouche et al., 2006). In this territory, numerous seismic sequences took place over the past decade (2012–2021), particularly around the Lesser Kabylia Block (LKB) (Fig. 1b). These include the 2017 seismic sequences along the Mçid Aïcha-Debbagh Fault (MADF) in the south (Bendjama et al., 2021), the 2014 Ziama and 2019 Jijel earthquakes in the north (Yelles-Chaouche et al., 2021), and the 2012–2013 Bejaia-Babors sequences in the west (Boulahia et al., 2021).

On January 24, 2020, at 07 h 24 m 20 s, the region of Jijel was shaken once more by a shallow earthquake of magnitude Mw 5.0, namely, the El Aouana earthquake at the western boundary of the LKB, 20 km southwest of Jijel (Fig. 1c). The western transverse fault system of Bejaia-Babors constitutes a NW–SE-trending structure associated with right-lateral strike-slip earthquake focal mechanisms. Recent advances in understanding the fault geometry mechanism in this region have been obtained by Boulahia et al. (2021), who identified the majority of the currently known en echelon fault segments that define the western boundary of the transverse fault system. The El Aouana 2020 earthquake exhibits a focal mechanism with one of the planes subparallel to the eastern boundary of the transverse fault system.

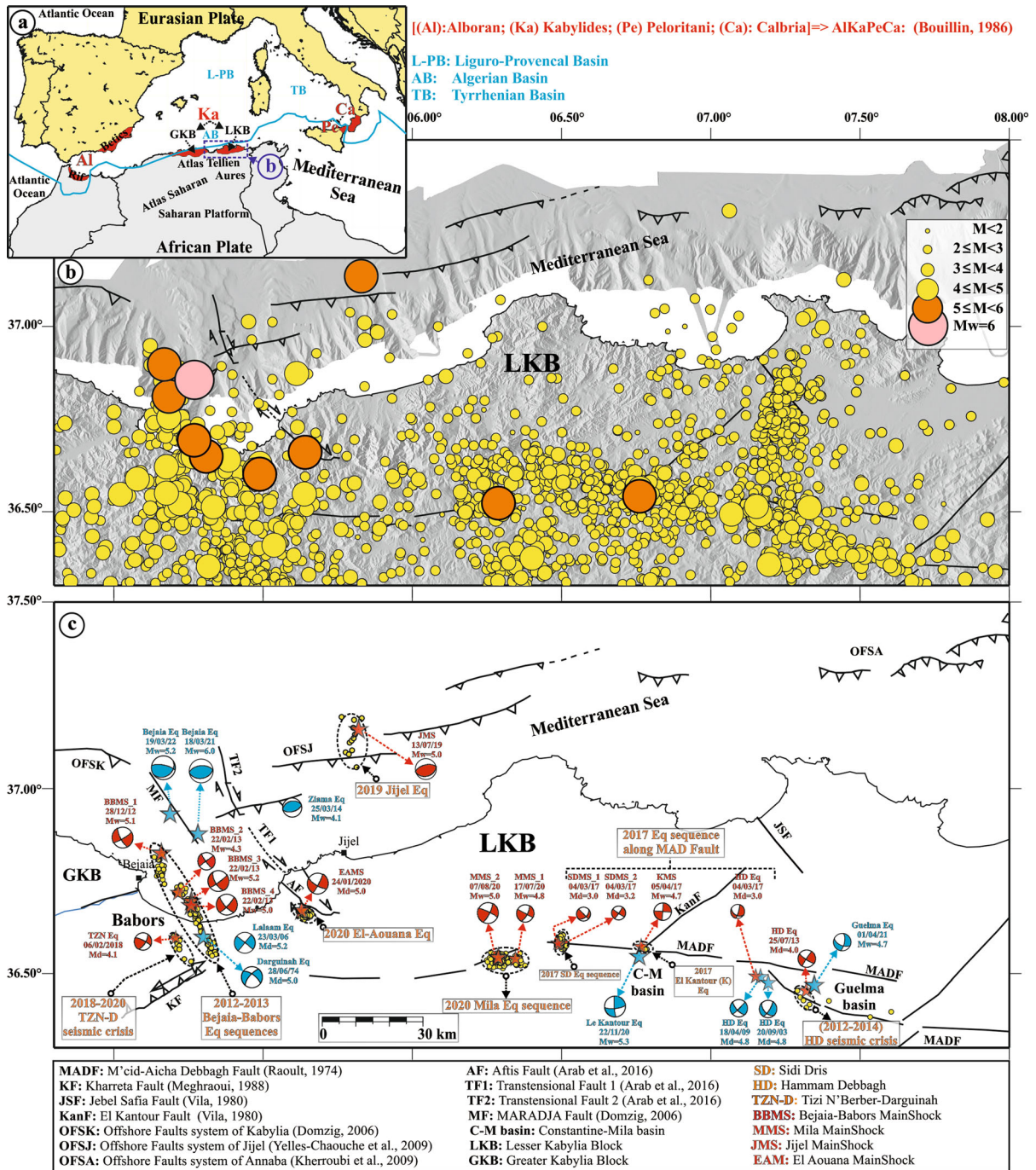


Figure 1

a Generalized map of the occidental Mediterranean, outlining the AlKaPeCa units (red color) along the current African-European plate boundary. The blue line denotes the Eurasia–Africa Plate boundary (simplified from Bird, 2003). **b** Seismicity in the LKB region is plotted with filled circles retrieved from CRAAG seismic catalogs for the 2007–2020 period. All main recent events of $M \geq 5$ until 2022 are also shown. **c** Map of the potential main active seismic structures (Domzig, 2006; Kherroubi et al., 2009; Meghraoui, 1988; Vila, 1980). The main recent seismic sequences (2012–2021) and specific mainshock focal mechanisms are also shown. The BTF, TDF, and LF (red lines) are the three fault segments determined by the aftershock distribution (Abbas et al., 2019; Boulahia et al., 2021)

Analysis of this sequence and review of largely recent studies present an opportunity to construct a thorough fault geometry model. Uncovering the fault zone geometry is essential to understanding how faults evolve and the mechanics of earthquake rupture.

Transcurrent faults never occur as simple planar faults through the crust. Instead, they define composite fault zones or brittle–ductile shear zones characterized by braided, parallel, or en echelon faults that are not perfectly straight (Sylvester, 1988). Since tectonic activity along shear zones frequently occurs over extended periods of time, these zones grow in width and length mainly following a process of segment linkage that typically generates heterogeneous and composite zones characterized by anastomosing patterns (Fossen & Cavalcante, 2017). The fault damage zone is the volume of deformed wall rocks around a fault core or slip surface resulting from incipient strain localization prior to fault formation or fault propagation, occurring during slip accumulation on nonplanar faults, and as a result of various types of fault interactions, which provides valuable information regarding fault initiation, propagation, and growth, as well as earthquake initiation and termination (Jin & Kim, 2020 and references therein). Therefore, a variety of accommodation structures can develop (Poli & Renner, 2004). Figures 1c and 2 show the various structures belonging to the NW–SE dextral strike-slip faults in the study area. The mapped traces of strike-slip faults are commonly characterized by discontinuities that appear as steps in map view (Wesnousky, 1988). Linking damage zones evolve between the interacting tips of adjacent faults (Kim et al., 2001). Bends and stepovers occur along all strike-slip systems (e.g., Christie-Blick & Biddle, 1985; Crowell, 1974a, 1974b), thereby creating zones of compression (restraining bends) and tension (releasing bends). As the fault displacement is increased through repeated earthquakes, they are also likely to grow in length (Jackson 1996). Therefore, in this study, we proposed a theoretical model of fault growth that attempts to explain several empirical observations.

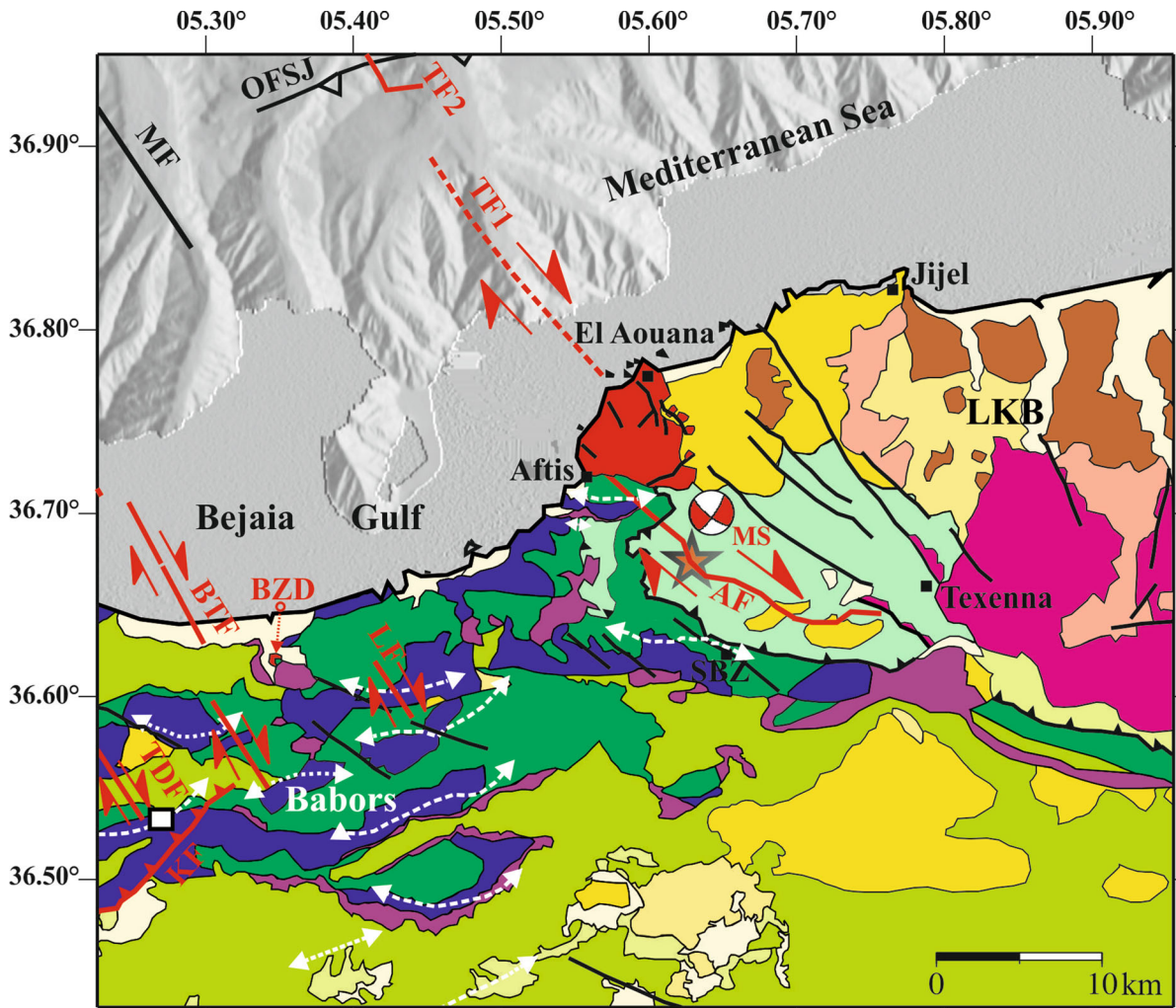
In this paper, the spatial and temporal evolution characteristics of precisely relocated aftershocks are documented, the fault architecture is defined, the transverse fault segments within a dextral Riedel

shear zone are examined, and the segmented fault evolution is finally modeled, thereby reconciling the results of this study and previous works.

2. Geological and Seismotectonic Settings

2.1. Geological and Tectonic Framework

The El Aouana region is located at the western end of the LKB, and this block resulted from the breakup of the Alboran microplate (Andrieux et al., 1971), formerly situated at south European margins. It is also known as AlKaPeCa (Bouillin et al., 1986), which encompasses the following peri-Mediterranean blocks, from west to east: (1) the Alboran system formed by the Betics and Rif in Spain and Morocco, respectively; (2) the Kabylides block formed by the Greater and Lesser Kabylia Blocks (GKB and LKB, respectively) in Algeria; (3) the Peloritani block in Sicily; and (4) the Calabria block in southern Italy (Fig. 1a). The Kabylides zone involves rigid Paleozoic metamorphic units belonging to the internal domain of the Maghrebides chain. Following Alpine deformation and metamorphism, these blocks migrated to their current locations during the opening of the Algerian, Liguro-Provençal and Tyrrhenian basins (A, L-P, and T, respectively, in Fig. 1a) by closely following an E–W extension direction (Alvarez et al., 1974; Bouillin, 1986; Cohen, 1980; Dewey et al., 1989). The Kabylides blocks collided and overthrust the external domain of the African margin during the Oligocene–early Miocene (Durand-Delga, 1969). In eastern Algeria, the LKB overthrust the para-autochthonous Tellian sedimentary units of the Babors chain (Kirèche, 1993). The LKB behaves as a rigid block; (1) this finding is supported by geologic observations (Durand-Delga, 1969), and (2) significant seismicity is lacking within the block (Fig. 1b), whereas historical and instrumental seismicity (2012–2021) are concentrated around the block (Fig. 1c) (Abacha et Yelles-Chaouche et al., 2019; Boulahia et al., 2021; Bendjama et al., 2021); moreover, (3) active deformation is manifested at the LKB borders (Bendjama et al., 2021; Bougrine et al., 2019; Yelles-Chaouche et al., 2021).



Stratigraphy		Main tectonic features
	Quaternary	
	Pliocene	
	Post-nappe Miocene	
	Post-nappe igneous rocks	MS: The 2020 El Aouana mainshock
	Numidian nappe	SBZ: Selma Ben Ziada
	Kabylian Oligo-Miocene	BTF: Babors Transfer Fault
	Eocene	TDF: Tizi N'berber-Darguinah Fault
	Flysh nappes	LF: Lalaam Fault
	Upper Cretaceous	AF: Aftis Fault
	Lower Cretaceous	MF1 and TF2: Transtentional Faults
	Jurassic	KF: Kherrata Fault
	Triassic	OFSJ: Offshore Faults System of Jijel
	Kabylian basement	BZD: Bou Zazen diorite
	Cu-Ag-Fe Mineralization	

◀Figure 2

Geologic setting of the western part of the LKB and Babors zone. Stratigraphic contours are obtained from Vila (1980) and Kirèche (1993), black tectonic features are obtained from Vila (1980) for the LKB, from Kirèche (1993) for Babors, and from Domzig (2006) for the offshore area. Red active faults (BTF and TD) are retrieved from Boulahia et al. (2021); LF is retrieved from Abbes et al. (2019); and AF, TF1 and TF2 are retrieved from Arab et al. (2016); while fold axial traces are shown as white dashed lines (Kireche, 1993)

The structural framework of the epicentral area is related to successive tectonic phases since the Oligocene, leading to the juxtaposition of the LKB with the Babors external domain. The main contact between the LKB and Babors chain is buried under a thick stack of gravitational thrust sheets andolistostromes (Fig. 2). Following the main thrusting event, the area experienced an extension phase expressed in the El Aouana zone as the emplacement of a prominent massif of intrusive and extrusive igneous rocks along the main fault (Villemaire, 1988). The extension phase was followed by a significant contraction period, as expressed by the reactivation of multiple basement strike-slip and thrust faults (Guiraud, 1977; Vila, 1980). Many of these faults are currently known as active structures, such as the newly identified (Boulahia et al., 2021) NW–SE Babors transfer fault system and the N70E Kherrata fold-related fault (KF) (Meghraoui, 1988; Rothé, 1950). The contact between the LKB and Babors chain is underlined by several NW–SE strike-slip faults affecting the postthrust sheet framework (Arrab et al., 2016; Robin, 1970; Vila, 1980), as documented in the El Aouana igneous massif (Villemaire, 1988). Kirèche (1993) also mapped multiple NW–SE faults in the Selma Ben Ziada area. The offshore part of this system (the Bejaia Gulf, a part of the Algerian basin) constitutes a back-arc basin, where a Mio-Pliocene sedimentary series was deposited atop a substratum of a laterally variable origin and nature. This basin evolved within the framework of dextral transtension, which was governed by a network of strike-slip faults with a normal extension component that generally ran NW–SE (Arab et al., 2016).

2.2. *Seismotectonics of the LKB*

The LKB is surrounded by several active faults. The seismicity associated with the northern end of the LKB has been poorly constrained for decades due to the lack of marine investigations and a satisfactory seismic network coverage. This area is characterized by an approximately E–W offshore thrusting fault system (OFS) stretching from Bejaia to Annaba (Domzig, 2006; Kherroubi et al., 2009; Yelles-Chaouche et al., 2009) and accommodates 1.5 mm/y of the entire Africa–Eurasia plate convergence (Bougrine et al., 2019). Prior to two recent earthquakes, no seismic activity has been reported along these faults since the 1856 Djidjelli earthquake of $I_0 = X$, which triggered a moderate tsunami in the western Mediterranean region. These two $M_w \geq 4.1$ events comprise the first instrumental signature of seismic activity in the Jijel margin. The first event, with a magnitude of $M_w 4.1$, occurred 20 km northwest offshore Jijel on March 25, 2014, while the second event, with a magnitude of $M_w 5.0$, occurred 40 km north of Jijel on July 13, 2019 (Fig. 1b and c). These events were generated by two approximately E–W thrust fault segments belonging to the offshore fault system (OFS) of the Jijel margin (Yelles-Chaouche et al., 2009, 2021) (OFSJ, Fig. 1b). West of the OFSJ, two important events were recorded in the Bejaia Gulf on March 18, 2021, and March 19, 2022, with magnitudes of $M_w 6.0$ and 5.2 , respectively. Their focal mechanisms revealed \sim E–W thrust faults, likely the western continuity of the OFSJ (Fig. 1b). Furthermore, Domzig (2006) mapped a NNW–SSE-striking fault off the Bejaia Gulf as part of the MARADJA project, which we refer to here as the MARADJA Fault (MF).

The southern LKB border corresponds to the \sim E–W-trending Moid Aicha Debbagh Fault (MADF), extending > 80 km from the Moid Aicha Massif north of Mila to the Debbagh Massif north of Guelma (Raoult, 1974). A recent study prolonged the fault to Gharimadou in Tunisia by more than 400 km and named it the Gharimadou–North–Constantine Fault (GNCF) (Bougrine et al., 2019). This major structure is characterized by transpression (Meghraoui & Pondrelli, 2012) and accommodates 44% of the total shearing, which results in a slip deficit rate of

2.4 mm/y (Bougrine et al., 2019). The fault zone is characterized by multiple small events and high b values (Abacha, 2015). It appears that the MADF comprises several small segments that reduce the effective normal stress and yield high b values, which provides favorable conditions for triggering small to moderate earthquakes. Several seismic sequences occurred along the MADF during the 2017–2021 period. The seismic sequence in 2017 occurred in three distinct areas (El Kantour, Sidi Dris, and Hammam Debbagh, Fig. 1b), culminating in an Mw 4.7 event in El Kantour (Bendjama et al., 2021). The 2020 Mila earthquake sequence was located at the western end of the MADF near the Beni-Haroun Dam and was characterized by the occurrence of two main Mw 4.8 and 5.0 shocks on July 17 and August 07, 2020, respectively. The third event, with a magnitude of Mw 5.3, struck the El Kantour region near the 2017 event on November 22, 2020 (Fig. 1b). Finally, in the Guelma pull-apart basin (the south-eastern end of the LKB), a Mw 4.7 earthquake occurred on April 1, 2021 (CRAAG).

At the western limit of the LKB, a newly identified NW–SE right-lateral transfer fault (Boulahia et al., 2021) crosses the whole Babors Mountains and Bejaia Gulf. This fault zone consists of (1) the Babors Transverse Fault (BTF), which caused the 2012–2013 Bejaia-Babors earthquake sequences, (2) the Tizi N'Berber-Darguinah Fault (TDF), which produced the 2017–2020 seismic crisis, (3) the Lalaam Fault (LF), which generated the 2006 Lalaam earthquake (Beldjoudi et al., 2009), and the NNW–SSE offshore active fault (Domzig, 2006). These fault segments jointly constitute a transfer zone relying on the OFS in the north and the MADF system in the south (Boulahia et al., 2021). Geological field investigations near the El Aouana region have revealed a NW–SE right-lateral strike-slip fault (denoted as the Aftis Fault or AF) (Arab et al., 2016), which is more likely to have hosted the 2020 El Aouana seismic sequence, the subject of this study (Figs. 1c and 2). The seismic interpretation procedure was applied to a 2D seismic dataset (Arab et al., 2016), which shows a potential offshore extension of the AF through two NW–SE dextral strike-faults (TF1 and TF2) exhibiting an extensional component, i.e., transtensional kinematics.

The eastern LKB boundary corresponds to the NW–SE Jebel Safia Fault (JSF) of Quaternary age, associated with active hydrothermal sources (Abacha et al., 2022; Harbi et al., 2003; Vila, 1980), and characterized by swarm-like seismic activity (i.e., without a clear mainshock). The eastern limit also coincides with a major 35 km long NW–SE-trending tectonic feature, the El Kantour Fault (KanF in Fig. 1c), exhibiting left-lateral strike-slip motion (Marre, 1992; Raoult, 1974).

3. Methodology

3.1. Data Acquisition

To acquire data in our study, we retrieved the 2020 El Aouana mainshock and early aftershocks from the Algerian Digital Seismic Network (ADSN) database. Prior to installing portable stations, the first locations were affected by significant errors, since the nearest station (CDFR) situated 30 km away from the epicentral zone and the gap reached $\sim 180^\circ$ (Fig. 3a). To reduce the gap and the distances to the aftershocks, we deployed, as a first step, four mobile stations along the coast (SP01, SP02, SP03, and SP04), installing SP01 in El Aouana city 28 h after the mainshock. As a second step, we added three more stations (SP05, SP06, and SP07) to surround the region affected by seismic activity.

The seven stations of the temporary network were equipped with Omnirecs CUBE3 24-bit digitizers and Mark Products L22 three-component sensors ($f_c = 2.0$ Hz), augmented with solar panels, and operated in continuous acquisition mode at a sampling rate of 100 Hz. A summary of the recording periods at each portable station is shown in Fig. 3b, which shows that the maximum number of phase readings was obtained at the SP04 station installed in Salma Ben Ziada village.

3.2. Data Processing

To determine the absolute locations of the 360 events collected over 3 months since January 24, 2020, we employed the widely used program HYPONVERSE2000 (Klein, 2002) using manually

picked phases P and S. The program also requires a 1D velocity model and Vp/Vs ratio. We investigated the determination of P-to-S velocity ratios using the modified Wadati method (Chatelin, 1978), with which the slope of S-waves of differential travel times ($TS_i - TS_j$) can be computed versus the corresponding P-waves ($TP_i - TP_j$) for all station pair combinations (i, j). A minimum 1D velocity model can be obtained by simultaneous inversion of arrival time data for hypocenter locations, seismic velocities, and station corrections (Kissling et al., 1994). Primarily, we used the Jijel wide-angle seismic profile as an a priori model (Mihoubi et al., 2014), located ~ 12 km east of the epicentral zone (Fig. 3b). Second, we provided a good-quality subset of available events, meeting the criteria of a maximum root-mean-square (RMS) value of 0.2 s and maximum horizontal (ERH) and vertical (ERZ) error values of 2 km, resulting in 306 events. The obtained velocity model consists of three layers whose P-wave velocities range from 5.5 to 7.1 km/s over the 0–20 km depth range (Fig. 4a). The computed Vp/Vs ratio is 1.76 (Fig. 4b). To refine the cluster of absolute locations, we applied a double-difference relocation procedure using the HypoDD algorithm (Waldhauser & Ellsworth, 2000), which employs both a catalog of P&S arrivals and cross-correlation time delays. The uncertainties associated with the relocation process were estimated using a bootstrap resampling method (Efron, 1982).

To compute focal mechanisms, we implemented the SPHERA routine (Rivera & Cisternas, 1990). With the use of the highest initial motion of P-wave polarities, we calculated 45 aftershock focal mechanisms and that of the mainshock. These 46 focal mechanisms were further used to analyze stress orientations and magnitudes using the Win-Tensor program (Delvaux, 2012).

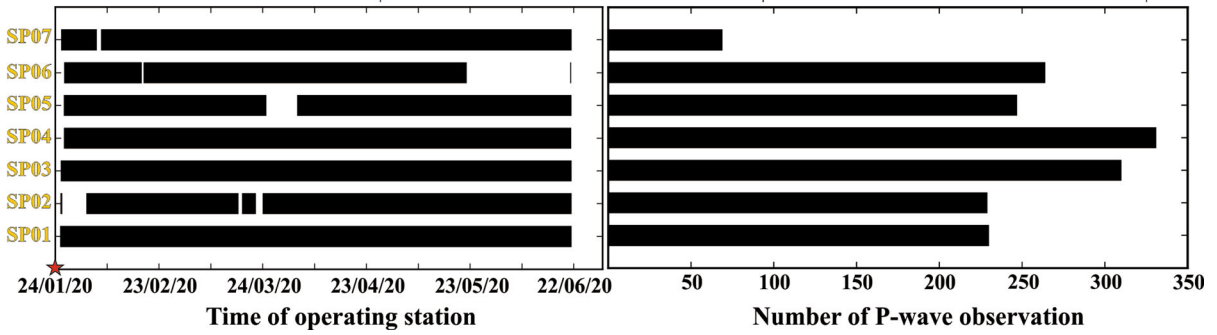
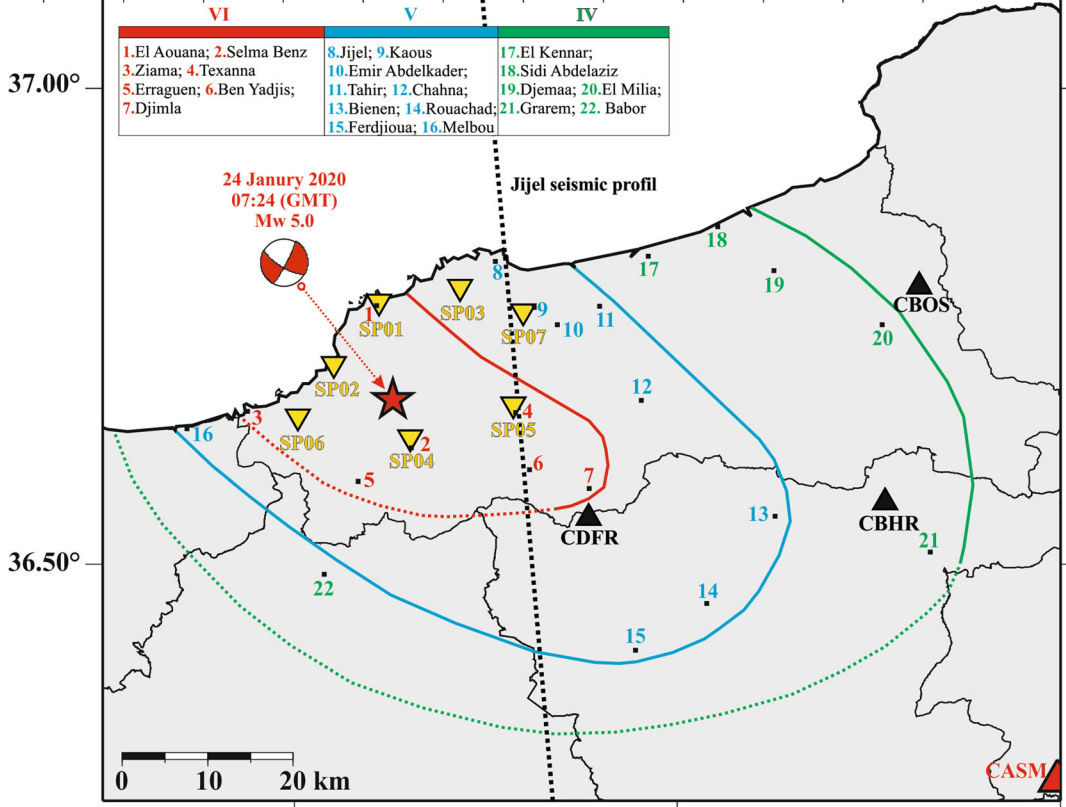
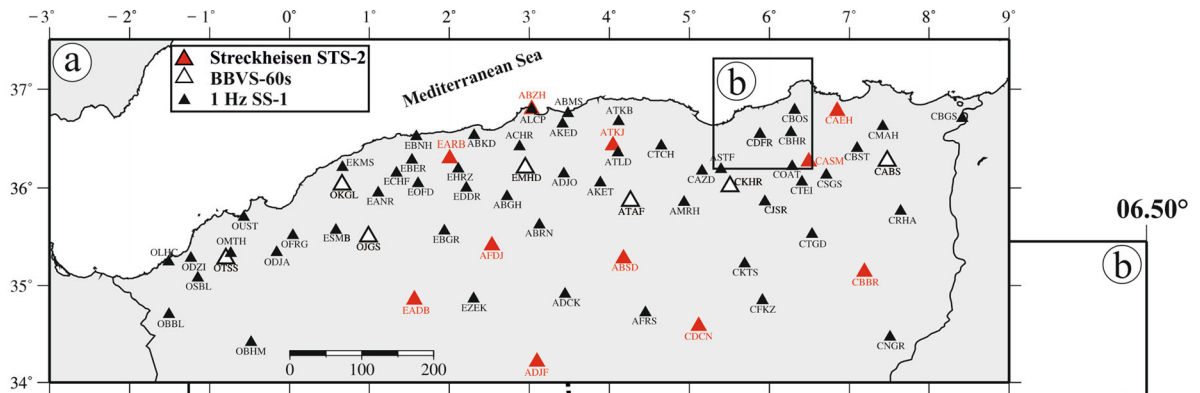
The source parameters of the two largest events were estimated using the waveform modeling method (Yagi and Nichimura 2011), which provided the moment tensor, seismic scalar moment M_0 , moment magnitude Mw, and nodal planes. Hence, ten three-component broadband stations and eight vertical-component short-period stations were operated (Figs. 3a and Appendix Fig. A1). The observed raw

data, 38 components in total, were corrected for instrumental responses and converted into ground velocity motion. Of the waveform data, the data from 100 to 180 s were split for each studied shock. The data were filtered at relatively low frequencies (0.02–0.07 Hz) to mitigate the local velocity structure heterogeneity effect and produce the optimal fit between the observed and synthetic waveforms (Appendix Fig. A1). The data were also downsampled to a 1 Hz rate. Green's functions of the synthetic seismograms were calculated using the discrete wavenumber method developed by Kohketsu (1985). The goodness of fit between the synthetic and observed data was measured by minimizing the variance factor.

The source parameters of the two largest events were additionally estimated using spectral analysis, as described in Abacha et al. (2019), and this method is based on a circular seismic source model (Brune, 1970, 1971). The MATLAB code selects, the low-frequency displacement spectral level Ω and the corner frequency f_c that minimize the variation between the theoretical and observed displacement spectra were selected. The average seismic moment, source radius, and stress drop values were then estimated using the formulae of Archuleta et al. (1982)

To model the occurrence rate of aftershocks in this sequence, we applied the restricted epidemic-type aftershock sequence (RETAS) stochastic model (Ogata, 1998), which is based on a specific branching process in which each event belonging to any given generation may produce offspring independent of the other shocks. This stochastic point process model considers the seismic activity in a given area to consist of two components: the independent background seismicity rate modeled by a stationary Poisson process with a constant occurrence rate μ and the aftershock occurrence rate. The conditional intensity function, $\lambda(t)$, of the RETAS model is the sum of these two components, which can be expressed as:

$$\lambda(t) = \mu + \sum_{\{i, t_i < t\}} \lambda_{(i)}(t) = \mu + \sum_{\{i, t_i < t\}} \frac{K}{(c + t - t_i)^p} e^{a(M_i - M_c)}, \quad (1)$$



◀Figure 3

a The permanent ADSN seismic stations include Geodevice BBVS-60 (white triangle) and Streckeisen STS-2 (red triangle) broadband sensors coupled to Geodevice EDAS-24IP and Quanterra (Kinometrics) Q330 digitizers, respectively, as well as 1 Hz Kinometrics SS-1 Ranger seismometers coupled to Quanterra Q330 digitizers (black triangle). Red broadband stations used for moment tensor inversion and spectral analysis. The black box outlines the study area. **b** Macroseismic map of the 2020 El Aouana mainshock with the locations of the seven portable stations. The station operation time schedule and the number of P phase pickings for each station are shown at the bottom left and right, respectively. The black dotted line indicates the location of the SPIRAL Jijel profile (Mihoubi et al., 2014)

where K , c , p , and α are constants, M_i is the magnitude of each event that occurred at time t_i and M_c is the completeness magnitude. In this study, the five parameters μ , K , c , p , and α were estimated.

The key feature between the RETAS and the ETAS models is that the first one provides a better fit to the temporal distribution. The ETAS model assumes that events in the sequence with magnitude $M \geq M_c$ (maximum curvature) are capable of producing a secondary aftershock. In contrast, the RETAS model is well known for the constraint that only aftershocks of magnitude greater than or equal

to some threshold M_{tr} can cause secondary events. By changing the triggering threshold, we analyzed the RETAS model modifications, including limit-case models like the Modified Omori Formula (MOF) and the ETAS model. With so many models available, we may choose the one that most accurately depicts an aftershock sequence (Gospodinov and Rotondi 2006).

4. Results

4.1. Mainshock: Macroseismic Assessment, Moment Tensor and Source Parameters

A moderate earthquake of magnitude M_D 4.8 occurred on January 24, 2020, at 07:24 (UTC) and impacted a region where Algerian catalogs reported several historical and recent events, particularly in the Babors region. The mainshock caused minor damage to the villages of El Aouana and Selma Benziada and their surroundings, provoking mainly superficial cracks in buildings of low-quality materials and a few mountain rockfalls far from populated areas. Based on the reported effects, we estimated a maximum intensity of VI (European Macroseismic Scale 1998). The generated isoseismal map, based on field investigation and eyewitness reports, shows a

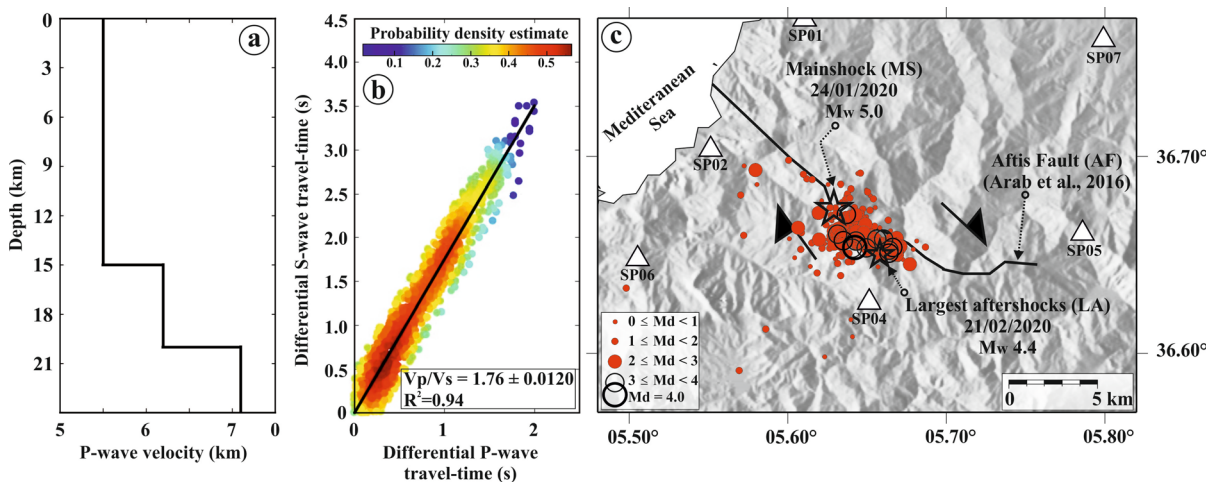







Figure 4

a Velocity model calculated by VELEST (Kisslig, 1994) using 306 well-located events, where Jijel's seismic profile (Mihoubi et al., 2014) was selected as an a priori model. **b** V_p/V_s ratio in the Beni-Illman area via the modified Wadati method (Chatelain, 1978). **c** Horizontal distribution of the 306 accurately located events. The main fault (denoted as the Aftis Fault or AF in this study) is reproduced from Arab et al. (2016)

Table 1
Focal mechanisms of the January 24, 2020, El Aouana mainshock, as determined by different seismological agencies

Agencies	Date	Origin time	Magnitude	Epicenter		Depth (km)	Nodal Plane 1			Nodal Plane 2			M ₀ (N.m)	Solution
				lat (°N)	lon (°E)		strike (°)	dip (°)	rake (°)	strike (°)	dip (°)	rake (°)		
CRAAG (this study) P-waves polarities	2020-01-24	07:24:17.03	M _D = 5.0	36.67	5.63	07.5	127.8	74.5	-167.9	34.5	78.4	-15.9	-	
CRAAG (this study) MT inversion	2020-01-24	07:24:17.03	M _w = 5.0	36.67	5.63	07.5	296.3	82.7	-176.6	205.9	86.6	-7.4	3.6 10 ¹⁶	
GFZ	2020-01-24	07:24:19.20	M _w = 4.9	36.76	5.61	11.0	120.0	72.0	-171.0	28.0	82.0	-17.0	-	
INGV	2020-01-24	07:24:20.60	M _w = 4.9	36.77	5.61	10.0	130.0	59.0	-168.0	34.0	80.0	-32.0	3.1 10 ¹⁶	
GCMT	2020-01-24	07:24:19.40	M _w = 5.1	36.72	5.57	18.0	125.0	62.0	-170.0	31.0	81.0	-29.0	5.3 10 ¹⁶	

general NW–SE trend (Fig. 3b). The mainshock location (5.65°E; 36.63°N), 20 km southwest of Jijel city, as computed by the ADSN, indicates slight discrepancies relative to foreign seismological agencies (e.g., GFZ, INGV, and GCMT) (Table 1).

The focal mechanism (FM), which we computed from the P-wave first motion polarities of 36 permanent station vertical components, showed a left-lateral strike-slip movement for the nodal plane oriented N034°E and a right-lateral strike-slip movement for the nodal plane oriented N128°E, remarkably matching the moment tensor solution well (Appendix Fig. A1), as well as the solutions of different agencies: GFZ, INGV, and GCMT (Table 1). We obtained the greatest variance reduction (89%) between the observed and synthetic seismogram waveforms at a 7 km source depth, yielding a seismic moment of $M_0 = 3.6 \times 10^{16}$ Nm, corresponding to Mw 5.0. We obtained equivalent results for the seismic moment after examination of 33 spectra retrieved from eleven three-component broadband stations (Appendix Fig. A2). Spectral analysis allowed us to calculate an average f_c value, seismic moment M_0 , source radius r , stress drop $\Delta\sigma$, multiplicative error factors (EM_0 and Ef_c), mean moment magnitude M_w , and average displacement U , all of which are listed in Table 2. The source parameters of the sequence largest aftershock (M_w 4.4) were also estimated using both waveform meddling (Appendix Fig. A1) and the spectral analysis method (Table 2).

4.2. Aftershock Distribution and Spatiotemporal Evolution

The aftershock distribution of the 306 selected events (Fig. 4b) indicated a main cluster 6 km long and 3 km wide and oriented NW–SE. This agrees with (1) the N128°E fault plane solution of the mainshock and (2) the apparent orientation of

isoseismal curves, and (3) the fault plane orientation matches that of the Aftis Fault (AF) in Arab et al. (2016), which is a NW–SE right-lateral strike-slip fault.

The histograms of the number of events (Fig. 5a) show 513 events (gray bars) detected by at least one station (SP04) and 360 events locatable by at least 3 stations (red bars). The ratio of 70% remains acceptable, which indicates that the epicentral zone is well covered by a tight temporary network.

The seismic activity lasted approximately 70 days from the date of the mainshock event on January 24, 2020 (MS event in Fig. 5a), during which the largest aftershock (LA in Fig. 5a) was recorded on February 22, 2020 (28 days). Following the occurrence of the mainshock, we observed an increase in aftershocks during the first 4 days (~ 220 cumulative events), followed by a decrease over the next 7 days, which may correspond to the first subsequence. On February 05, 2020 (13 days), we noted a second burst of events with a peak of 29 recorded events on February 02, 2020 (10 days), followed by a decrease over the next 7 days, which probably corresponds to a second subsequence. Finally, the small peak of fifteen events observed on February 19, 2020 (27 days), could mark the beginning of a third subsequence, of which the main peak was recorded two days later with 60 events, including the largest aftershock (LA), occurring the day after a rapid decay was clearly observed.

The number of events consecutively increasing and decreasing suggests that secondary aftershocks triggered their own aftershocks; therefore, we employ the RETAS model to examine the temporal distribution of aftershocks. This model states that earthquakes with magnitudes $M \geq M_{tr}$ (the threshold magnitude) can trigger secondary aftershocks. To fit the model, a threshold magnitude (M_{tr}) equal to 2.0 was selected according to the best AIC. Figure 5b displays the RETAS-fit for the cumulative number of

Table 2

Average corner frequency (f_c), seismic moment (M_0), source radius (r), stress drop ($\Delta\sigma$), multiplicative error factors (EM_0 and Ef_c), and mean values of the moment magnitude (M_w) and displacement (U) for the 2020 El Aouana mainshock event (MS) and its largest aftershock (LA)

Event	Date	f_c (Hz)	Ef_c	M_0 (N.m)	EM_0	$\Delta\sigma$ (MPa)	r (m)	U (m)	M_w
MS	2020-01-24	1.26	1.07	$3.9 \cdot 10^{16}$	1.18	3.96	1624	0.16	5.0
LA	2020-02-21	1.89	1.10	$5.0 \cdot 10^{15}$	1.24	1.74	1082	0.05	4.4

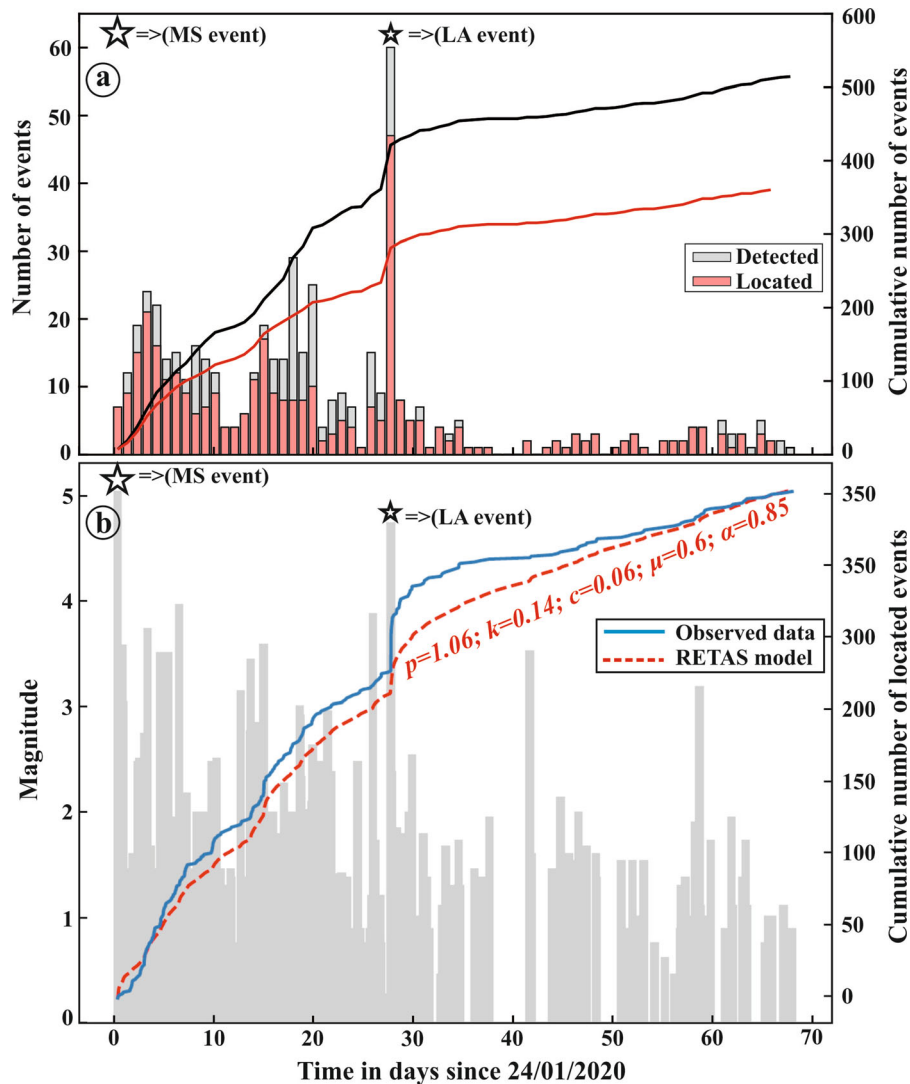


Figure 5

a Number and cumulative number of detected and located events per day. **b** Best-fit ETAS model for the cumulative number of events above magnitude M 2.0 for the 2020 El Aouana earthquake. p , k , α , μ and c are the RETAS constants

earthquakes and the optimal values of the model parameters (P , K , c , μ , and α).

4.3. Event Relocation, Focal Mechanisms and Stress Tensor

The 306 located events were used to extract travel time differences between the manually picked data, applying the following criteria: a maximum number of 10 neighbors, a maximum separation distance of 5 km, and for a given pair, a minimum number of

eight (08) links. We ran the relocation procedure using only catalog data and then computed cross-correlations involving the relocated event seismograms. We were successful in relocating 291 out of 306 events, which were then cross-correlated across all available stations. The waveform similarity between events was calculated using a normalized time domain cross-correlation, with a minimum cross-correlation threshold of $CC = 0.7$. As shown in the Appendix (Fig. A3), an example of high waveform similarity ($CC \geq 0.8$) was obtained for

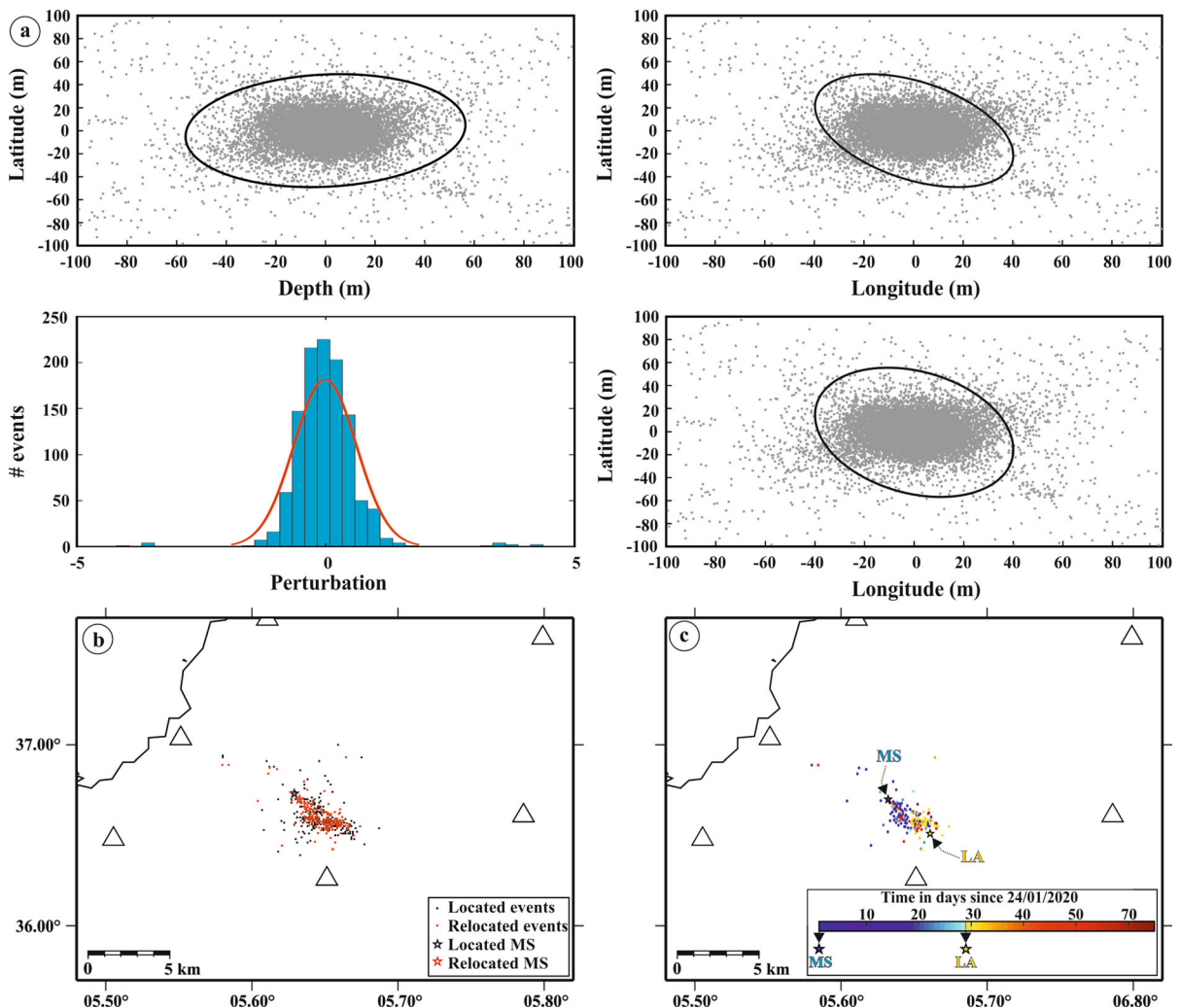


Figure 6

a Location uncertainty estimation, the contour indicates the 95% confidence ellipsoid x (E–W), y (N–S), and z (up–down), with normally distributed noise for the P phase. **b** Overlaid of 204 relocated events (red dots) and their located pairs (black dots). **c** Spatiotemporal evolution of the relocated events

two groups of events recorded at stations SP01 and CDFR. Cross-correlation P-wave travel time delays were then associated with P- and S-wave delays computed from the manually picked arrival times to relocate 204 out of 291 events.

To estimate the uncertainty associated with the relocation process, we used the bootstrap resampling method by generating normally distributed noise of a zero mean and a standard deviation appropriate to the dataset. We perturbed the pair's differential times and then relocated them. This process was repeated 200

times, accumulating 204×200 epicenters, which are shown in Fig. 6a. The relative errors along the three directions x (E–W), y (N–S), and z (up–down) are ~ 40 m, ~ 50 m, and ~ 60 m, respectively.

The improvement in the horizontal distribution is shown in Fig. 6b by overlying the 204 relocated events and their located pairs. The spatial distribution of relocated aftershocks allowed us to differentiate one NW–SE-oriented cluster. The aftershock spatiotemporal evolution shows (Fig. 6c) that the aftershock zone expanded toward the SE along the

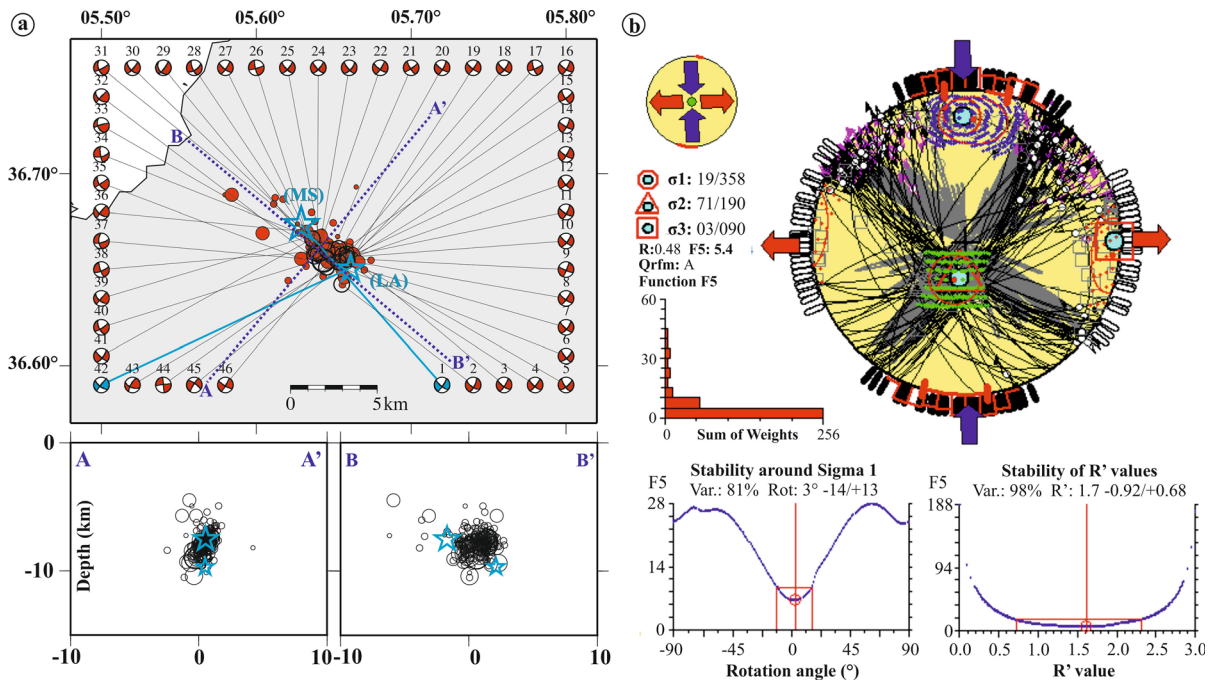


Figure 7

Horizontal and vertical distributions of the 204 relocated events of the 2020 El Aouana earthquake, showing 44 focal mechanisms of events with $M \geq 2$ and 2 focal mechanisms of events with $M < 2$. The focal mechanisms are numbered as in Table 3, and their polarities are shown in Appendix Fig. A4. **b** Stress inversion result showing selected focal planes projected (black lines) onto the lower hemisphere (Schmidt stereographic projections) with the three principal stress axes (σ_1 : circle, σ_2 : triangle, and σ_3 : square) and horizontal stress axes (S_{Hmax} : blue arrows; S_{Hmin} = green arrows). The stress symbols indicate the horizontal stress axes. The histogram shows the distribution of the misfit function F5, linearly weighted by the event magnitude. QRfmt is the quality ranking of the focal mechanism solutions for stress data records from formal stress inversions

fault strike, beginning rapidly after the MS. During the 28 days between the Mw 5.0 MS and the Mw 4.3 LA, the aftershocks migrated from the rupture zone of the MS to the epicenter of the LA and continued to expand toward the SE. Cross sections (A-A' and B-B', Fig. 7a) indicated that the 5–10 km deep foci were mostly distributed on a quasivertical plane, striking NW–SE, dipping 75° to the SW, and exhibiting an approximate length of 5 km and width of 2 km. All focal mechanisms (Table 3, Fig. 7a and Appendix Fig. A4) indicated that one of the nodal planes, trending NW–SE, matched the relocated event spatial distribution (horizontal and vertical).

To determine the third-order stress field in the study area, we inverted all 46 focal solutions (92 nodal planes in Fig. 7b) of the 2020 El Aouana earthquake. The selected nodal planes are moderately to steeply inclined ($60\text{--}90^\circ$) with NW–SE- and NE–

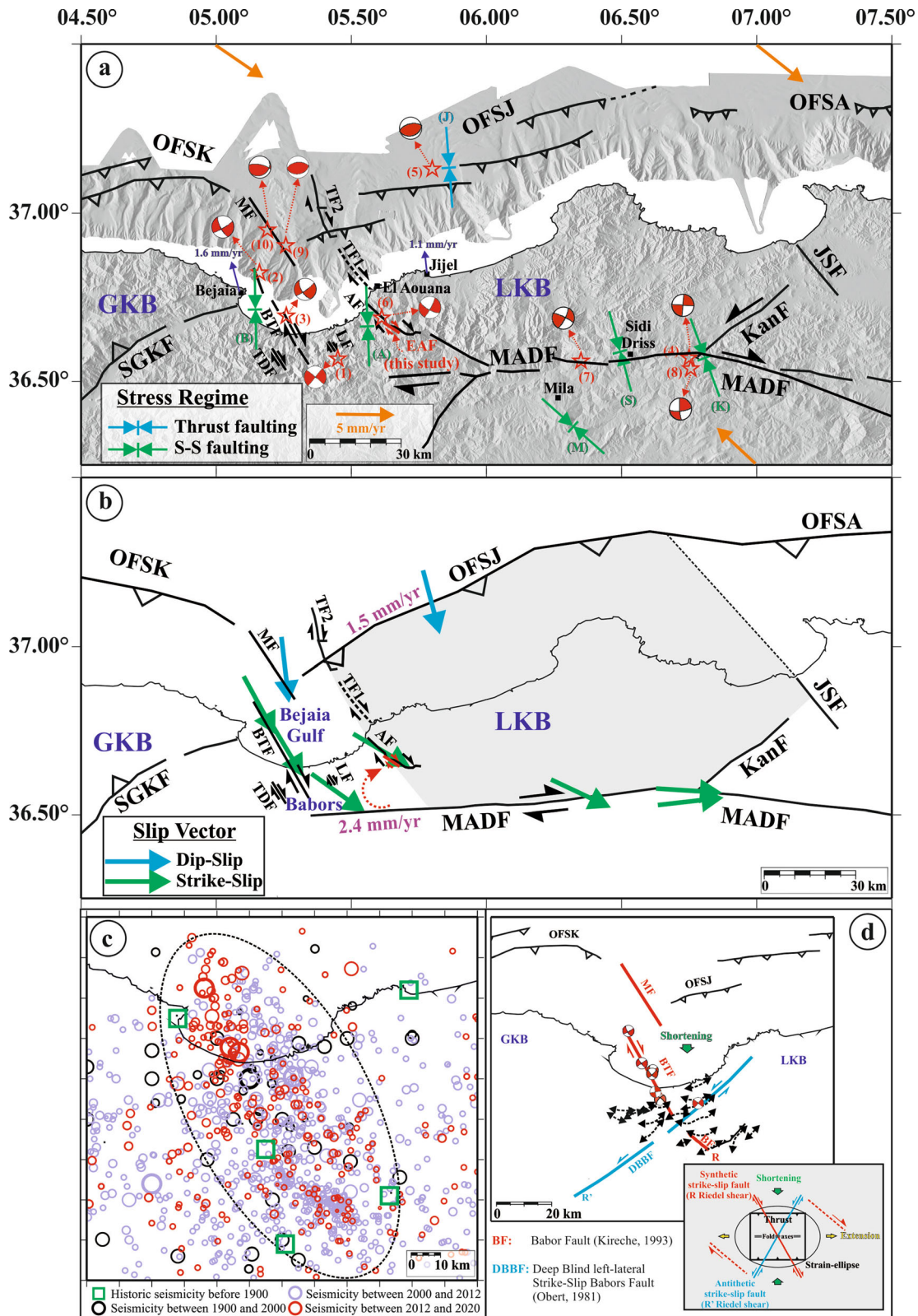
SW-striking planes. The two focal planes defined in Fig. 7b are consistent with a N-S-oriented maximum horizontal principal stress ($S_{Hmax} = N179^\circ \pm 12.1^\circ$). The average slip deviation is 5.4, the quality can be ranked 'QRfm = A' excellent, and the waveform misfit function $F5 = 10.6$ indicates that the solution is well constrained. The tensor comprises a subvertical $\sigma_2 = 71/190$, subhorizontal $\sigma_1 = 19/358$, and $\sigma_3 = 03/090$. The stress regime index ($R' = 1.52 \pm 0.46$) indicates a pure strike-slip regime according to the classification of Delvaux et al. (1997). These results suitably agree with those of previous stress studies around the LKB (Bejaia-Babors (Boulahia et al., 2021), the Jijel region (Yelles-Chaouche et al., 2021), and the MADF region (Bendjama et al., 2021)).

Table 3

Fault plane solutions for the mainshock event and the 45 key aftershocks

N°	Date	Origin time	M _D	Epicenter		Depth km	Nodal plane 1			Nodal plane 2			Score	Quality
				lat (°N)	lon (°E)		strike (°)	dip (°)	rake (°)	strike (°)	dip (°)	rake (°)		
1	2020-01-24	07:24:17	5.0	36.670	5.632	7.53	34.5	78.4	-15.9	127.8	74.5	-167.9	84.2	64.5
2	2020-01-24	11:25:03	3.8	36.642	5.655	9.38	26.8	72.4	-24.4	124.6	66.8	-160.8	85.3	67.0
3	2020-01-27	08:06:59	3.7	36.658	5.658	7.42	125.8	72.2	-167.9	32.1	78.5	-18.2	100	71.0
4	2020-01-28	16:26:49	3.1	36.660	5.646	7.75	131.2	75.1	-169.3	38.5	79.6	-15.1	100	70.0
5	2020-01-29	10:20:37	3.5	36.657	5.656	7.59	49.9	71.5	-18.3	145.9	72.7	-160.6	100	73.1
6	2020-01-30	13:52:35	4.0	36.655	5.643	9.00	47.0	68.2	-12.7	141.7	78.3	-157.7	100	71.6
7	2020-01-31	07:52:06	2.2	36.654	5.650	8.28	37.5	71.3	-14.2	132.1	76.5	-160.8	100	74.0
8	2020-02-02	21:52:04	2.5	36.657	5.645	7.58	34.4	81.8	-14.6	126.5	75.6	-171.5	100	75.0
9	2020-02-03	09:02:03	2.5	36.656	5.653	7.98	112.9	82.1	-174.7	22.2	84.8	-7.9	100	70.3
10	2020-02-05	19:37:00	3.2	36.656	5.658	8.04	38.0	73.7	-11.0	131.2	79.4	-163.5	100	74.0
11	2020-02-06	17:42:53	2.8	36.657	5.659	7.99	27.4	77.8	-17.3	121.2	73.1	-167.2	100	72.8
12	2020-02-06	20:01:11	3.5	36.655	5.659	7.97	139.4	76.6	-166.7	46.3	77.1	-13.8	100	75.1
13	2020-02-06	20:36:36	2.4	36.656	5.659	8.18	30.7	82.3	-14.2	122.7	75.9	-172.0	100	71.6
14	2020-02-06	21:42:56	2.8	36.655	5.661	7.69	119.9	78.5	-168.0	27.5	78.3	-11.7	100	72.1
15	2020-02-06	22:09:25	2.2	36.657	5.650	8.02	52.9	76.2	-16.9	147.0	73.6	-165.7	100	72.4
16	2020-02-07	03:30:50	2.4	36.656	5.660	8.00	29.5	77.3	-16.9	123.4	73.5	-166.7	100	73.2
17	2020-02-07	09:52:43	2.6	36.656	5.660	7.60	160.6	73.3	-167.9	67.1	78.4	-17.1	100	75.4
18	2020-02-07	15:09:44	2.2	36.657	5.658	7.55	130.4	73.1	-164.4	35.7	75.0	-17.5	100	75.2
19	2020-02-07	16:49:38	2.9	36.655	5.661	7.81	35.0	81.6	-12.8	126.9	77.3	-171.4	100	77.6
20	2020-02-07	22:04:09	2.5	36.659	5.653	7.48	29.4	76.2	-15.9	123.3	74.6	-165.6	82.9	66.9
21	2020-02-07	22:13:48	2.0	36.654	5.646	8.99	56.2	82.5	-11.5	147.7	78.6	-172.3	87.5	67.7
22	2020-02-08	02:59:58	2.4	36.664	5.642	9.08	33.0	79.8	-17.2	126.2	73.1	-169.3	100	72.5
23	2020-02-08	04:08:16	3.6	36.658	5.640	8.97	42.4	65.3	-16.0	139.2	75.5	-154.4	95.8	71.2
24	2020-02-08	04:11:06	2.2	36.661	5.639	7.99	42.0	77.4	-15.2	135.4	75.2	-166.9	100	74.2
25	2020-02-08	04:29:49	2.5	36.658	5.642	7.96	135.3	74.3	-165.8	41.4	76.3	-16.2	100	73.6
26	2020-02-08	04:53:13	2.8	36.658	5.636	8.85	74.9	82.9	-12.2	166.4	77.9	-172.8	100	66.8
27	2020-02-08	05:13:51	3.5	36.658	5.639	8.32	127.9	73.4	-168.3	34.5	78.8	-16.9	92.9	71.3
28	2020-02-09	01:45:37	2.0	36.660	5.640	8.05	157.6	67.8	-152.6	56.5	64.8	-24.7	100	68.5
29	2020-02-10	05:38:16	2.3	36.659	5.638	8.49	142.6	37.0	-160.6	36.9	78.5	-54.6	100	65.8
30	2020-02-11	02:32:27	1.6	36.654	5.652	9.14	136.9	62.0	-167.8	41.1	79.2	-28.6	100	65.2
31	2020-02-11	02:56:34	2.0	36.663	5.642	7.86	160.2	56.4	-166.7	62.7	78.9	-34.4	100	75.0
32	2020-02-11	19:58:31	3.0	36.651	5.645	8.44	222.6	87.0	35.9	130.5	54.2	176.3	100	70.2
33	2020-02-12	00:35:59	2.4	36.655	5.651	8.12	253.7	79.7	40.2	155.1	50.6	166.6	100	67.4
34	2020-02-13	02:05:05	2.1	36.658	5.662	7.39	171.2	78.5	-154.6	75.8	65.1	-12.7	100	72.0
35	2020-02-13	04:10:03	2.7	36.656	5.629	9.31	146.4	62.7	-179.5	56.2	89.5	-27.3	100	75.0
36	2020-02-13	23:51:20	2.5	36.670	5.632	9.07	126.0	62.6	174.0	218.8	84.7	27.5	100	63.5
37	2020-02-14	16:36:22	2.9	36.654	5.658	9.51	176.3	61.2	-159.1	75.9	71.8	-30.5	100	66.0
38	2020-02-15	00:58:25	2.4	36.659	5.638	8.41	159.8	77.9	-166.5	66.9	76.8	-12.5	100	69.7
39	2020-02-16	02:55:22	1.4	36.668	5.638	7.34	220.3	88.5	29.8	129.4	60.2	178.2	100	71.2
40	2020-02-17	17:45:48	2.5	36.657	5.648	8.16	154.4	61.9	-165.5	57.4	77.3	-28.9	100	73.2
41	2020-02-19	07:32:49	3.9	36.666	5.636	8.65	131.3	77.6	-161.9	37.3	72.3	-13.0	100	72.8
42	2020-02-21	02:55:17	4.7	36.651	5.661	9.69	218.2	85.4	21.3	126.4	68.8	175.1	97.7	65.5
43	2020-02-21	03:05:36	2.2	36.658	5.663	7.65	210.0	74.7	30.7	111.1	60.5	162.3	100	73.1
44	2020-02-21	03:25:30	2.4	36.656	5.654	7.42	173.6	89.8	175.5	263.6	85.5	0.2	100	70.8
45	2020-02-21	03:39:40	2.6	36.656	5.662	7.34	212.6	80.7	-15.5	305.2	74.7	-170.3	100	74.0
46	2020-02-22	23:55:59	2.0	36.657	5.649	8.18	121.2	79.0	-174.1	30.0	84.2	-11.0	100	73.6

N° event number, Date event date, M_D duration magnitude. Strike, Dip and Rake are the three parameters of the nodal plane. Score and quality are two parameters that measure the similarity between observed and model-predicted polarities



◀Figure 8

a Seismotectonic map of our study area, displaying the main active faults (inspired by Raoult (1974), Domzig (2006), Kherroubi et al. (2009), Vila (1980), Arab et al. (2016), and Boulahia et al. (2021)) as well as the focal mechanisms of recent earthquakes of $M \geq 5$. The stress symbols indicate the S_{Hmax} orientations (B: Bejaia; A: El Aouana; J: Jijel; S: Sidi Driss; K: El Kanteur and M: Mila regions). GPS velocities are shown relative to the Eurasia plate (purple arrows). General plate vector (orange arrows) shown with respect to Eurasia (top) and Nubia (bottom) from Bougrine et al. (2019). **b** Horizontal projections of the slip vectors of the main recent events. **c** Seismic events detected in the region from 1900 to 2020 and the largest historical earthquakes (CRAAG catalog). **d** Model of the horizontal strain ellipse where the R Riedel shear (Riedel, 1929) corresponds to the right-lateral shear zone

5. Discussion

5.1. Transverse Fault System Architecture and Its Role in Strain Partitioning

The 2020 El Aouana seismic sequence deepened our understanding of the active tectonics of the LKB and Babors zone and was recently brought to light through the analysis of seismic events and sequences between 2012 and 2020 (Boulahia et al., 2021; Yelles-Chaouche et al., 2021). The aftershock distribution of the El Aouana earthquake revealed a NW–SE right-lateral strike-slip fault ~ 6 km in length denoted as the El Aouana Fault (EAF). The projection of the EAF to the surface agrees with the AF (Arab et al., 2016) (Fig. 8a). The AF fault bounds the LKB to the west and lies within a transverse zone that extends from Bejaia to Babors. Between the LKB and GKB, the GKB eastern boundary includes several NW–SE-trending right-stepping strike-slip fault segments: the BTF, TDF, LF, and the active NNW–SSE MARADJA (MF) offshore fault (Boulahia et al., 2021).

The abovementioned transverse fault system plays a fundamental role in strain partitioning. Indeed, the present strain partitioning in northeastern Algeria results from NW–SE-directed Eurasia–Africa plate convergence, involving two major fault structures bounding the LKB to the north and south (Fig. 8). The northern edge corresponds to the Jijel offshore thrust fault system (OFSJ) associated with a slip deficit rate of 1.5 mm/y, whereas the southern edge coincides with the E–W MADF master fault along

which dextral displacement accommodates a significant present-day slip deficit rate estimated at ~ 2.4 mm/y (Fig. 8b) (Bougrine et al., 2019). The oblique convergence was spatially partitioned into orthogonal slip (thrusting) and dextral strike-slip (shearing) motion components around the LKB, whereas in the GKB, thrust slip vectors were subparallel to the overall NW–SE Eurasia–Africa motion, suggesting no partitioning; thus, all convergence was accommodated by shortening along faults and thrust folds. In several regions worldwide subjected to oblique convergence, the strain between converging blocks is commonly partitioned into nearly pure thrust faulting on some faults and nearly pure strike-slip faulting on other subparallel faults (Berberian et al., 1992; Jackson, 1992; Talebian & Jackson, 2002). Furthermore, slip vectors calculated from recent main focal mechanisms (Fig. 8b) support partitioning; the slip vectors of strike-slip FMs are subparallel to the MADF and BTF, while those of inverse FMs are perpendicular to the OFSK and OFSJ. The transition from partitioning (LKB) to no or much less partitioning (GKB) along a given zone of strike-slip motion necessitates a NW–SE transverse fault system, connecting the MADF master fault in the south and the offshore fault system in the north. This transition can be achieved by right-lateral strike-slip faults and overall related clockwise rotations about vertical axes (the red circular arrow in Fig. 8b).

5.2. Bejaia-Babors Shear Zone

The transverse fault system separating the GKB and LKB likely delineates a 30–35 km wide NW-trending shear zone, hereafter referred to as the Bejaia-Babors Shear Zone (BBSZ). The EAF fault, identified in this study, combined with literature review, revealed surface evidence of a plausible BBSZ:

- (1) Geophysical and geodetic evidence
According to Reuther et al. (1993), transitional areas, generally between regions of different crustal thicknesses and different modes of continental crust underthrusting, are incipient zones of strike-slip, oblique or normal motion to the

collisional front. In this case, between the GKB and LKB, a crustal thickness disparity was observed in seismic profiles during the Maradja2/Samra 2005 survey (Déverchère et al., 2005). With the use of previous data, a structural map of the eastern Algerian submarine margin was generated (Domzig, 2006). On the map, a network of thrust faults was shaped in overlapping steps, expressed by asymmetric folds in topographic and bathymetric reliefs (Fig. 8a). The thrust faults were all south-dipping faults, some of which controlled the uplift of a rollover hanging wall offshore the GKB; in contrast, folds and rollovers were poorly developed offshore the LKB, perhaps due to a later onset of tectonics and therefore less strain in this area (Domzig, 2006). Regarding underthrusting crust inhomogeneity, a differential deformation velocity of 0.5 mm/y was identified between the GKB and LKB based on measurements retrieved from the Bejaia (GKB) and Jijel (LKB) GPS stations, respectively (Bougrine et al., 2019) (Fig. 8a).

(2) Geomorphic evidence

The concave shape on the bathymetric relief map and on the OFSK thrust upon approaching the MF (Fig. 8a) is consistent with dextral shearing along the NW-trending BBSZ.

(3) Offshore neotectonic evidence

In the Bejaia Gulf, a NNW–SSE lineament was interpreted by Harbi et al. (1999) and Domzig (2006) as a Pliocene–Quaternary fault, illustrated as MF in Fig. 8. The two NW–SE oriented strike-slip faults with normal components, represented as TF1 and TF2 in Fig. 8, are active faults following Arab et al. (2016).

(4) Onshore geologic evidence

In the Babors area, dextral strike-slip faults affect Jurassic limestone belts (Fig. 2) by dragging and dextral shearing rock layers (Boulahia et al., 2021; Kirèche, 1993), similar to the previous OFSK drag fault indicated in Fig. 8a. Moreover, the BBSZ boundaries are delineated by magmatic rocks, ophiolitic fragments, and mineralization consistent with the presence of a complex shear or suture zone in the area. Indeed, along the eastern border, the recently recognized mafic and ultramafic ophiolitic complex of Texenna is

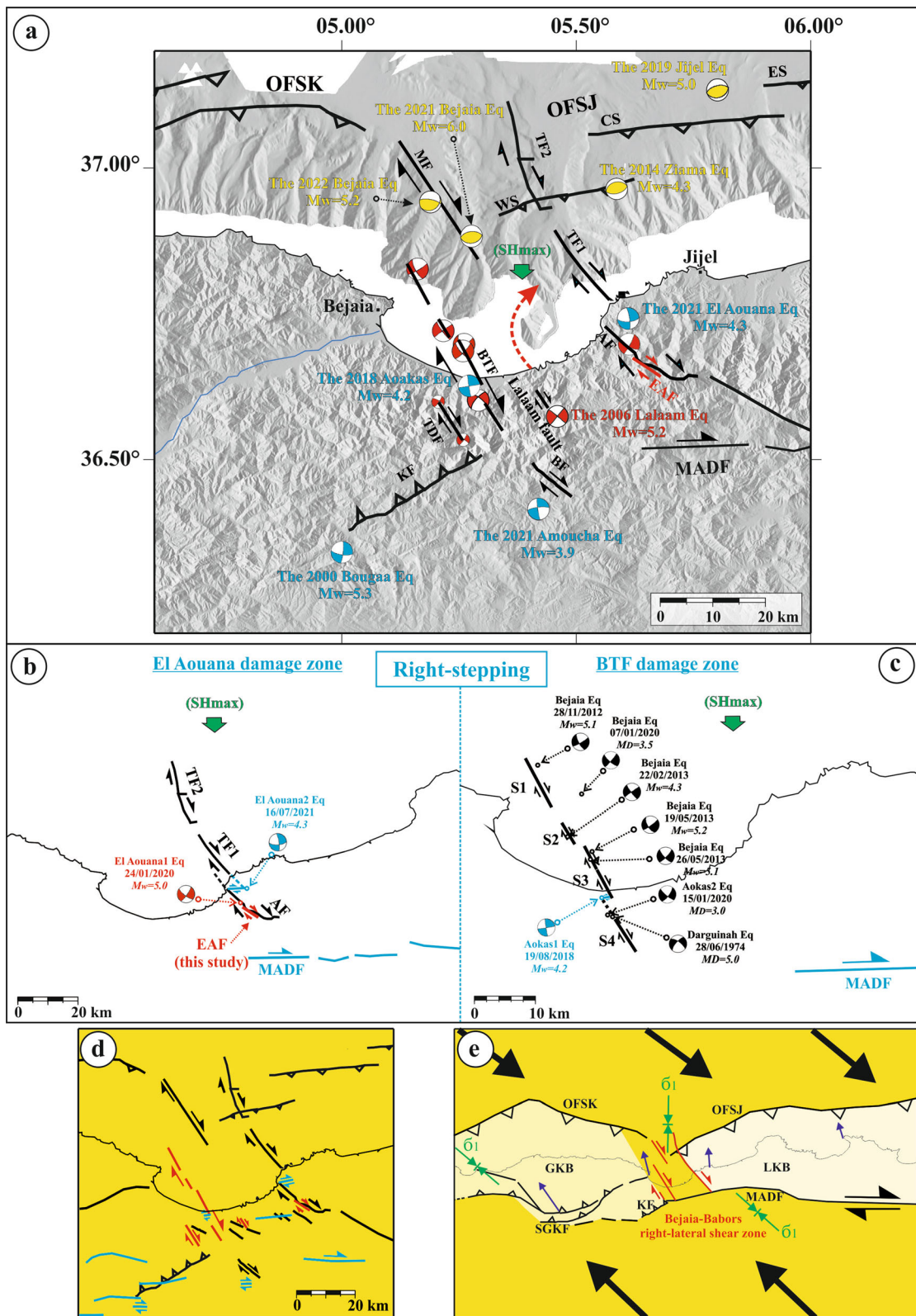
Figure 9

a Map of the current fault pattern supported by recent seismological data. The main active faults (Arab et al., 2016; Abbas et al., 2019; Boulahia et al., 2021; Domzig, 2006; Kherroubi et al., 2009; Meghraoui, 1988; Raoult, 1974; Vila, 1980;). Main focal mechanisms, where red denotes NW–SE right-lateral strike-slip faulting, blue denotes ~ E–W right-lateral strike-slip faulting, and yellow denotes ~ E–W thrust faulting. **b** Proposed model for the stepover areas in the El Aouana damage zone and the BTF damage zone (c). **d** Summary map of the shear zone. The NE–SW red lines denote the active faults determined by the aftershock distribution and focal mechanisms (Abbes et al., 2019; Boulahia et al., 2021, and this study). The ~ E–W right-lateral strike-slip segments marked in blue, which are located in the stepover region, are interpreted as preexisting structures. Some E–W-trending lineaments (blue lines) are also shown, duplicated from Meghraoui's geological map (Meghraoui, 1988). **e** The NW–SE Bejaia-Babors dextral shear zone (BTF, TDF, MF, LF, AF, and EAF) in a regional context. GPS velocities are shown relative to the Eurasia plate (purple arrows). The broad arrows indicate the general AF-EU plate oblique vectors

located in the southeastern continuity of the EAF fault (Boukaoud et al., 2021), whereas the El Aouana Miocene igneous complex (Chazot et al., 2017) is exposed just to the northwest of this fault (Fig. 2). Additionally, the western boundary of the BBSZ is characterized by the occurrence of ophiolitic fragments (gabbro and mafic lavas) (Obert, 1981), Miocene magmatic rocks (Bou Zazen diorite) (Kireche, 1993) and Triassic mélange material near the passage of the Babors transverse fault. Further south, manifestations of Cu–Ag–Fe mineralization (Tadergout and Beni Felkai mines) (Glaçon, 1967) are widespread near the passage of the Tizi N'Berber-Darguinah Fault (TDF) (Fig. 2). The BBSZ model presented here provides a reasonable explanation for these features, whose locations and orientations were previously poorly understood.

(5) Seismologic evidence

The overall seismicity cloud, for the 1900–2020 period, exhibits a major NW–SE trend (Fig. 8c) across the Babors mountain range and Bejaia Bay. With a width of approximately 30 km, it overshadows the BBSZ. Several key event focal mechanisms within the cloud also show NW–SE right-lateral strike-slip faulting (Abbes et al., 2019; Beldjoudi et al., 2009; Boulahia et al.,



2021), consistent with BBSZ shear movement. The seismogenic depth is concentrated in the upper crust, between 10 and 15 km, indicating that the BBSZ extends to at least 15 km. According to general knowledge of shear zones (Fossen & Cavalcante, 2017), lower crustal ductility may suggest downward widening of the BBSZ. However, the distribution of events alone is insufficient to draw any conclusions.

- (6) Rotation of the stress field and GPS velocities
 Within the BBSZ, the N–S maximum compression axis σ_1 (Fig. 7b and Boulahia et al., 2021) and GPS velocities (Bougrine et al., 2019) are rotated clockwise relative to NW–SE convergence of the African–Eurasian tectonic plates. The stress field is deflected around preexisting weak faults (Tingay et al., 2010; Yale, 2003). In the BBSZ, a major NW–SE strike-slip structure was inherited from the docking of the LKB and GKB blocks to the African continent (Schettino & Turco, 2006), and we suspect stress field rotation to favor slip along NW-trending structures.

5.3. Constraining of the Strain Ellipsoid in the BBSZ

The local tectonic regime of the Bejaia-Babors shear zone is a strike-slip regime (Fig. 7b and Boulahia et al., 2021). Several faulting types are likely to occur in a strike-slip shear zone. Considering the orientation of the maximum horizontal stress (σ_1 or S_{Hmax}) inferred in this study, we constructed an incremental strain ellipse for the Bejaia-Babors shear zone, as shown in Fig. 8d, with conjugate Riedel shear bands denoted as R and R'. The R-shears are synthetic to the sense of slip in the shear zone, forming right-stepping en echelon arrays along dextral shear zones and left-stepping arrays along sinistral shear zones. Here, R-shears are represented by the MF, BTF, TDF, LF, EAF, and AF faults. R'-shears may correspond to a deep blind left-lateral strike-slip fault of the Babors (DBBF in Fig. 8d), as identified by Obert, (1981); however, we have not yet registered seismological evidence supporting this trend. We observed a favorable correspondence between the thrust faults in the deformation ellipse

and the offshore faults in the zone, as well as the thrust folds onshore (Fig. 8d).

5.4. Origin and Evolution of Steppers Within the Shear Zone

We investigated steppers to better understand the interaction between overlapping fault segments within the BBSZ and to define tectonic development. The fault overlaps and their internal structures showed a high degree of scale independence and could be considered an anomalously wide and complex part of the fault damage zone (Fossen, 2020; Fossen et al., 2005; Kim et al., 2004). This differs from the damage zone at fault tips (McGrath & Davison, 1995) and along faults (ordinary fault-wall damage zones) (Caine et al., 1996).

Before starting the probe, Fig. 9a shows the main focal mechanisms according to the corresponding fault kinematics. We distinguished between (1) ~ E–W thrust FMs (yellow color) on OFSJ fault segments in the northern part, (2) NW–SE right-lateral strike-slip FMs (red color) associated with the BTF, TDF, LF, and EAF segments that constitute the studied shear zone, and (3) ~ E–W right-lateral strike-slip FMs (blue color), which are located in the steppers, as detailed below. The MF fault segment kinematics lacked the fault configuration depicted in Fig. 9a, but the fault is active according to Domzig (2006) and Harbi et al. (1999). Knowing that the NW faults in Algeria are generally right-lateral strike-slip faults, in addition to all fault segments compromising the transfer system indicating right-lateral motion, we may presume that the MF is also a right-lateral strike-slip fault, given its position within the transfer zone (Fig. 9a).

The steppers exhibited right-lateral motion on E–W structures (Fig. 9a). Several E–W faults were inherited from preexisting structures. Onshore, the active fault architecture in the northern Tellian Atlas of Algeria was formed as encompassing echelon-arranged thrust folds and associated strike-slip faults, dominated by NW–SE to E–W right-lateral strike-slip faults and NE–SW subordinate left-lateral faults. The major strike-slip structures were formed at the site of ancient large Mesozoic and Oligo-Miocene basins with high-angle normal faults reactivated during the

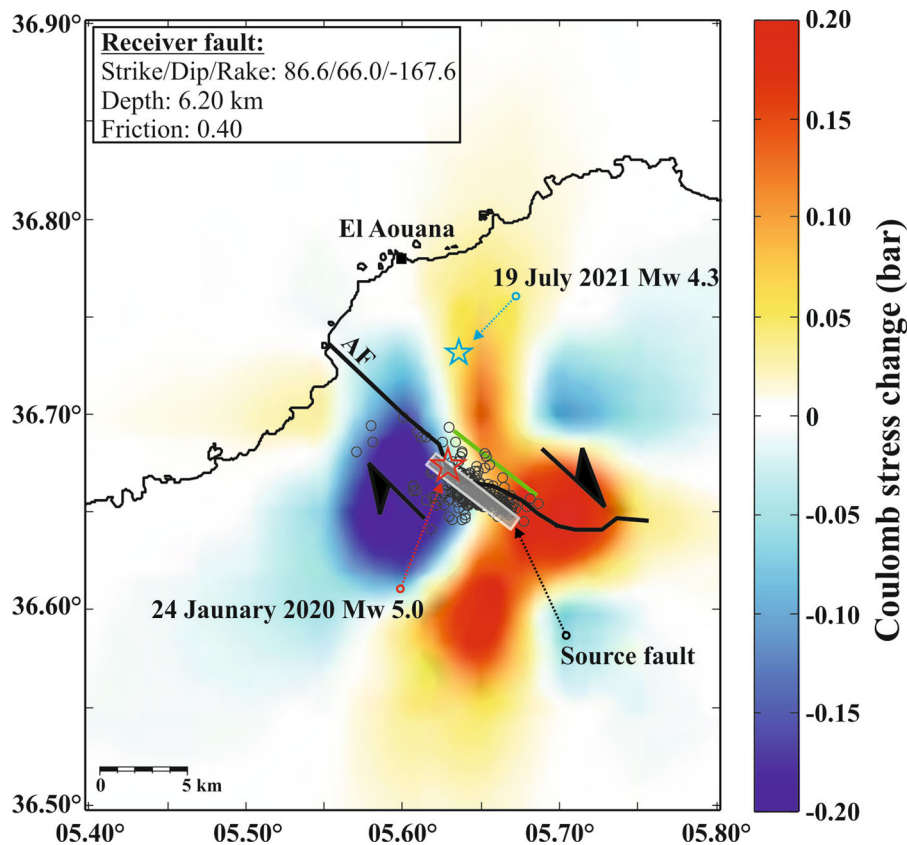


Figure 10

Coulomb stress change due to the NW-SE fault segment (strike: N128°E, dip: 74°, rake: -168°) on the E-W receiver fault segment (strike: N87°E, dip: 66° to SE, rake: -168°)

Cenozoic and Quaternary periods (Soumaya et al., 2018 and references therein). Offshore, the Algerian margin, situated in the western Mediterranean, is one of the few examples of a rifted margin subjected to compression and tectonically reactivated (Strzeczynski et al., 2010). The steep slope of the eastern Algerian margin is suggested to result from transcurrent motions during back-arc opening (Mauffret et al., 2004; Schettino & Turco, 2006). For example, off Jijel, the Ocean-Continent Transition zone (COT) is very close to the coast with a narrow width, which might be related to E-W opening of the basin (Klingelhoefer et al., 2022 and references therein). Thus, the stepover between the continental AF segment and its offshore extension segment TF1 (Fig. 9b) appears to be crosscut by an E-W structure, as indicated by an earthquake nodal plane. Indeed, on July 19, 2020, an earthquake of magnitude Mw 4.3 occurred in the El Aouana area, 5 km northeast

of the El Aouana sequence mainshock (Mw 5.0). The focal mechanism shows right-lateral movement on the E-W striking plane. To determine whether the static stress changes resulting from the Mw 5.0 event triggered the Mw 4.3 event, we calculated the Coulomb stress changes with the Coulomb 3.3 software package (Lin & Stein, 2004; Toda et al., 2005). The results (Fig. 10) showed that the rupture of the Mw 4.3 event occurred in an area of increased Coulomb stress, suggesting that the discharged Mw 5 zone triggered the Mw 4.3 event, which occurred in a critical failure state. Consequently, even moderate events could contribute to tectonic activity and therefore structural growth.

Additional events occurred along the E-W trend. On August 19, 2018, an earthquake of magnitude M_D 4.2 was accurately located in the Aoakas area, precisely between two BTF fault segments, the S3 offshore and S4 continental segments (Boulahia et al., 2021, Fig. 9c). As

previously stated, the focal mechanism shows right-lateral motion along the E-W-oriented fault plane (Fig. 9c). Most likely, it aided in splitting the BTF fault into the S3 and S4 segments. More recently, a compelling event occurred further southeast at the southern termination of the BF fault (Kirèche, 1993; Fig. 9a), which was an earthquake of magnitude Mw 3.9 that occurred in the Amoucha territory on November 28, 2021. The focal mechanism, as determined by P-wave onsets and waveform modeling, indicates right-lateral motion on the E-W plane. Likely, it represents the MADF western continuation, crossing the NW-SE shear zone structures (Fig. 9d). If the MADF continues westward, this would coincide with the (Mw 5.3) Bougaa earthquake in 2000 (Harvard-CMT; Figs. 9a and d). We showed (in Fig. 9d, thick blue line) E-W-trending structures cloned from Meghraoui's geological map (Meghraoui, 1988); unfortunately, their kinematics are unknown. It should be noted that the MADF western continuation remains unresolved to date (Bougrine et al., 2019). Our understanding of the fault architecture and kinematics in this region may evolve based on the insights provided in this work.

In classic extensional stepovers, a NE-SW-oriented connecting fault would be expected rather than an E-W-oriented connecting fault. However, as demonstrated in the preceding paragraphs supported by focal mechanisms, the slip orientation may be influenced by weak preexisting structures. The presence of older E-W structures could even constitute the origin of the NNW-trending fault segmentation. We should also remember that the E-W-striking MADF (or GNCF) played a significant role in the clockwise rotation of both the stress and velocity fields from NW-SE to ~ N-S (Boulahia et al., 2021), as well as possibly in the segmentation of the NNW-trending faults within the shear zone.

We could conclude from all available seismologic evidence that the BBSZ consists of several main NW-SE right-lateral strike-slip fault segments, including the AF and BTF faults, which are likely to form its eastern and western borders, respectively, and are segmented by E-W right-lateral connecting faults (Fig. 9d). The BBSZ is shown in Fig. 9e.

5.5. Sequence Spatiotemporal Evolution for Fluid-Driven Force Monitoring

In several previous studies, the role of fluids in the rupture process has been addressed (Bourouis & Cornet, 2009; Chen et al., 2012; Duverger et al., 2015). A recent study (Boulahia et al., 2021) unveiled the interplay between tectonic loading and fluids in the triggering of Bejaia-Babors aftershocks along the BTF. Is this also the case for the 2020 El-Aouana sequence? To answer this question, a spatiotemporal analysis was performed using the RETAS model.

The RETAS model was fitted for the period ranging from January 24, 2021 (mainshock day), to $T_d = 68$ days (Fig. 5b). One may notice that model adjustments for this period yielded poor fits. The computed $\alpha = 0.85$ indicates swarm-like activity, while a higher α value suggests mainshock-aftershock sequences (Ogata, 1988, 1998). However, it would be more reasonable if a high α value was found in this analysis, since El Aouana aftershock activity clearly indicated a mainshock-aftershock sequence. Additionally, Ogata (1998) established that conspicuous secondary aftershocks could lower the α -value, which is consistent with the seismic sequence studied. The fitted RETAS model yielded a low forcing rate of $\mu = 0.6$ events per day, leading to a total of approximately 40 earthquakes during the whole sequence period of 68 days. This indicates that only 14% of all earthquakes were externally triggered, while the great majority was self-triggered.

6. Conclusion

In this paper, we present the relocation results, spatiotemporal evolution characteristics, and focal mechanisms of the 2020 El Aouana seismic sequence that occurred in the western LKB limit. This sequence began on January 24, 2020, with a moderate (Mw 5.0) event and was followed by several aftershocks, including one event (Mw 4.4) on February 21, 2020. First, we identified the fault geometry and examined the tectonic role played within the transverse fault system. Then, we presented the arguments that support a wide NW-trending shear zone in the region (BBSZ), where the studied fault is part of its

eastern border. The BBSZ structures correlated well with Riedel shears. Finally, we examined the stepover origin and evolution within the BBSZ overlaps.

Both the national ADSN and the temporary deployed local network provided high-quality waveform data that allowed the identification and successful location of 360 events. Out of 360 events, 306 were defined as being of high quality based on specific criteria. The accuracy of El Aouana 2020 hypocenters was enhanced by applying a relative relocation method, yielding a total of 204 out of 306 events (66% of the events). The obtained RETAS parameters were significantly influenced by the conspicuous secondary aftershocks, making the investigation of fluid involvement in aftershock triggering inconclusive. We determined 46 FMSs revealing a NW–SE right-lateral strike-slip fault with a length of 6 km denoted as the El Aouana Fault (EAF), found to line up with a fault revealed in previous geological studies.

The EAF fault, located west of the LKB, lies within a transverse fault system that extends from Bejaia to Babors and includes several NW–SE trending right-stepping strike-slip fault segments: BTF, TDF, LF, and the active NNW–SSE MAR-ADJA (MF) offshore fault. Combined, they form a transfer zone between the E–W offshore thrusting fault system (OSF) and the subparallel major strike-slip fault (MADF) that accommodates and partitions strain from oblique convergence stress.

A review of previous studies in light of the findings in this study, especially geologic literature, pertaining to the Bejaia-Babors onshore and offshore parts provided evidence of a potential NW-trending Bajaia-Babors shear zone (BBSZ). The stepovers between the en echelon arranged NW–SE trending segments appeared to be influenced by inherited E–W structures, resulting in their current pattern.

All the NW–SE trending and tectonically active segments in the strain ellipse coincided with Riedel R-band shears. However, there is no seismologic evidence yet for R¹-bands, which may develop or be reactivated after the R-bands. The Riedel model was strengthened by thrust faults and folds within the BBSZ.

Present-day activity is well documented along the BBSZ, which shows predominantly right-lateral kinematics. The newly defined BBSZ is proposed as a

seismogenic source hosting fault segments characterized by evidence of present-day tectonic activity. Previous researchers considered the Kherrata reverse fault, located south of the BBSZ, as the source of Bejaia-Babors seismic activity. The BBSZ model presented is important to consider in future seismic hazard studies. Furthermore, the BBSZ itself must be thoroughly examined, particularly in the contact area between the lower crust and upper mantle.

Acknowledgements

During the review process, we were surprised by the news announcing the retirement of Prof. Abdelkarim Yelles-Chaouche. We dedicate this work to him, and may his retirement be as remarkable as his efforts in mentoring us. A special thanks to Editor Carla Filomena Braitenberg and two anonymous reviewers for their insightful comments on the original version of the paper. This work was supported by CRAAG, the department of seismology (Project ES-04-2020).

Author Contributions AI and HB conceived, interpreted the results, and wrote the main manuscript text. AI and OB collected the data. AI produced the figures and participated in the processing of data. OB, KR, and STR participated in the processing of data. HF and AYC reviewed the manuscript and participated in the interpretation of the results. MCC worked out the onshore geologic evidence in the discussion and YM wrote the geologic framework and prepared the geologic map. E-MT redid the relocations, estimated the relocation errors using bootstrapping, and analyzed the spatio-temporal evolution. CA helped in collecting permanent station records. All authors reviewed the manuscript.

Funding

No funding has been received from any organization.

Data Availability

The datum collected from the Algerian Seismological Network, which includes permanent and mobile stations, is primarily used by Algerian researchers. CRAAG, as a research center under the Algerian Interior Ministry, manages the country's national security, including natural hazards. CRAAG is not a

Data Management Center like well-known international centers such as IGN (Spain), but it has agreements and conventions with international agencies such as CESM, IGN, and ISC for data exchange, as per the ministry's policy. The data are also used for training young Algerian seismologists to build capacity and expertise in seismology within Algeria or for collaboration with foreign researchers under intra-institutional conventions. This supports Algeria's need for researchers and promotes advancement in the field of seismology.

Declarations

Conflict of interest The authors declare that they have no known competing financial interests or personal relationships that could have appeared to influence the results and/or discussion reported in this paper.

Publisher's Note Springer Nature remains neutral with regard to jurisdictional claims in published maps and institutional affiliations.

Springer Nature or its licensor (e.g. a society or other partner) holds exclusive rights to this article under a publishing agreement with the author(s) or other rightsholder(s); author self-archiving of the accepted manuscript version of this article is solely governed by the terms of such publishing agreement and applicable law.

REFERENCES

- Abacha, I. (2015). Étude de la sismicité de la région Nord-Est de l'Algérie, Thèse de Doctorat, Université Ferhat Abbas-Sétif (Algérie). <http://dspace.univ-setif.dz:8888/jspui/handle/123456789/1802>
- Abacha, I., Boulahia, O., Yelles-Chaouche, A., Semmane, F., Beldjoudi, H., & Bendjama, H. (2019). The 2010 Beni-Ilmane, Algeria, Earthquake Sequence: Statistical Analysis, Source Parameters, and Scaling Relationships. *Journal of Seismology*, 23(1), 181–193.
- Abacha, I., & Yelles-Chaouche, A. (2019). Overview of Recent Seismic Activity in Northeastern Algeria. In: Sundararajan, N., Eshagh, M., Saibi, H., Meghraoui, M., Al-Garni, M., Giroux, B. (eds) On Significant Applications of Geophysical Methods. CAJG 2018. Advances in Science, Technology & Innovation. Springer, Cham. https://doi.org/10.1007/978-3-030-01656-2_46
- Abacha, I., Yelles-Chaouche, A., & Boulahia, O. (2022). Statistical Study of Earthquake Swarms in Northeastern Algeria with Special Reference to the Ain Azel Swarm; Hodna Chain, 2015. In: Advances in Geophysics, Tectonics and Petroleum Geosciences. CAJG 2019. Advances in Science, Technology & Innovation. Springer, Cham. https://doi.org/10.1007/978-3-030-73026-0_34
- Abbes, K., Dorbath, C., Dorbath, L., et al. (2019). Revisiting the Laalam (Eastern Algeria) March 20, 2006 (Mw 5.1) Earthquake and its Seismotectonic Implication. *Pure and Applied Geophysics*, 176, 4213–4222. <https://doi.org/10.1007/s00024-019-02206-3>
- Alvarez, W., Coccozza, T., & Wezel, F. C. (1974). Fragmentation of the Alpine ergogenic chain by microplate dispersal. *Nature*, 248, 309–314.
- Andrieux, J., Fontbote, J. M., & Mattauer, M. (1971). Sur un modele explicatif de l'arc de Gibraltar. *Earth and Planetary Science Letters*, 12, 191–198. [https://doi.org/10.1016/0012-821X\(71\)90077-X](https://doi.org/10.1016/0012-821X(71)90077-X)
- Arab, M., Rabineau, M., Déverchère, J., Bracène, R., Belhai, D., Roure, F., Marok, A., Bouyahiaoui, B., Granjeon, D., Andriessen, P., & Sage, F. (2016). Tectonostratigraphic evolution of the eastern Algerian margin and basin from onshore-offshore correlation. *Marine and Petroleum Geology*, 77, 1355–1375.
- Archuleta, R. J., Cranswick, E., Mueller, C., & Spudich, P. (1982). Source parameters of the 1980 Mammoth Lakes, California, earthquake sequence. *Journal of Geophysical Research*, 87, 4595–4697.
- Beldjoudi, H., Guemache, M.A., Kherroubi, A., Semmane, F., Yelles-Chaouche, A.K., Djellit, H., Amrani, A., & Haned, A. (2009). The Laalam (Bejaia, North-East Algeria) moderate earthquake (Mw = 5.2) on March 20th, 2006. *Pure and Applied Geophysics* 166(4), 623–640
- Bendjama, H., Yelles-Chaouche, A.K., Boulahia, O., Abacha, I., Mohammedi, Y., Beldjoudi, H., Rahmani, S.T., Belheouane, O. (2021). The March 2017 earthquake sequence along the E-W-trending Mcid Aicha-Debbagh Fault, Northeast Algeria. *Geosciences Journal*. <https://doi.org/10.1007/s12303-020-0059-y> pISSN 1226-4806 eISSN 1598-7477
- Berberian, M., Qorashi, M., Jackson, J. A., Priestley, K., & Wallace, T. (1992). The Rudbar-Tarom earthquake of 20 June 1990 in NW Persia: Preliminary field and seismological observations, and its tectonic significance. *Bulletin of the Seismological Society of America*, 82(4), 1726–1755. <https://doi.org/10.1785/BSSA0820041726>
- Bougrine, A., Yelles-Chaouche, A. K., & Calais, E. (2019). Active deformation in Algeria from continuous GPS measurements. *Geophysical Journal International*, 217, 572–588. <https://doi.org/10.1093/gji/ggz035>
- Bouillin, J.P. (1986). Le "bassin maghrebin" ; une ancienne limite entre l'Europe et l'Afrique à l'ouest des Alpes, *Bull. Soc. Géol. Fr.*, II (4), 547–558.
- Bouillin, J.P., Durand-Delga, M., & Olivier, P. (1986). Betic-rifian and tyrrhenian arcs: Distinctive features, genesis and development stages. In: *Developments in Geotectonics*. Elsevier, pp 281–304
- Boukaoud, H., Godard, G., Chabou, M. C., Bouftouha, Y., & Doukkari, S. A. (2021). Petrology and geochemistry of the Texenna ophiolites, northeastern Algeria: Implications for the Maghrebain flysch suture zone. *Lithos*, 390–391, 106019. <https://doi.org/10.1016/j.lithos.2021.106019>
- Boulahia, O., Abacha, I., Yelles-Chaouche, A.K., Bendjama, H., Kherroubi, A., Mohammedi, M., Aidi, C., & Chami. (2021). Recent seismic activity in the Bejaia-Babors region (Northeastern Algeria): the case of the 2012–2013 Bejaia earthquake

- sequences. *Pure Appl Geophys.* <https://doi.org/10.1007/s00024-021-02711-4>
- Bourouis, S., & Cornet, F. H. (2009). Microseismic activity and fluid fault interactions: Some results from the Corinth Rift Laboratory (CRL), Greece. *Geophysical Journal International*, 178, 561–580.
- Brune, J. N. (1970). Tectonic stress and the spectra of seismic shear waves from earthquakes. *Journal of Geophysical Research*, 75, 4997–5009.
- Brune, J. N. (1971). Correction (to Brune 1970). *Journal of Geophysical Research*, 76, 5002.
- Caine, J. S., Evans, J. P., & Forster, C. B. (1996). Fault zone architecture and permeability structure. *Geology*, 24, 1025–1028.
- Chatelain, J.L. (1978) Etude fine de la sismicité en zone de collision continentale à l'aide d'un réseau de stations portables : la région Hindu-Kush-Pamir. Thèse de 3eme cycle, Univ. Paul Sabatier, Toulouse.
- Chazot, G., Abbassene, F., Maury, R. C., Déverchère, J., Bellon, H., Ouabadi, A., & Bosch, D. (2017). An overview on the origin of post-collisional Miocene magmatism in the Kabylies (northern Algeria): Evidence for crustal stacking, delamination and slab detachment. *Journal of African Earth Sciences*, 125, 27–41. <https://doi.org/10.1016/j.jafrearsci.2016.10.005>
- Chen, X., Shearer, P. M., & Abercrombie, R. E. (2012). Spatial migration of earthquakes within seismic clusters in Southern California: Evidence for fluid diffusion. *Journal of Geophysics Research*. <https://doi.org/10.1029/2011JB008973>
- Christie-blick, N., & Biddle, K.T. (1985). Deformation and basin formation along strike-slip faults. In: Biddle, K. T. & Christie-blick, N. (eds) Strike-Slip Deformation, Basin Formation, and Sedimentation. SEPM Special Publications, 37, 1–34.
- Cohen, C. R. (1980). Plate tectonic model for the Oligo-Miocene evolution of the western Mediterranean. *Tectonophysics*, 68, 283–311.
- Crowell, J.C. (1974a). Sedimentation along the San Andreas Fault, California. In: Dott, R. H. & SHAVER, R. H. (eds) Modern and Ancient Geosynclinal Sedimentation. SEPM Special Publications, 19, 292–303.
- Crowell, J.C. (1974b). Origin of late Cenozoic basins of southern California. In: Dickinson, W. R. (ed.) Tectonics and Sedimentation. SEPM Special Publications, 22, 190–204.
- Delvaux, D. (2012). Release of program Win-Tensor 4.0 for tectonic stress inversion: statistical expression of stress parameters. EGU General Assembly, Vienna, Apr. 22–27, EGU2012-5899.
- Delvaux, D., Moeys, R., Stapel, G., Petit, C., Levi, K., Miroshnichenko, A., Ruzhich, V., & San'kov, V. (1997). Paleostress reconstructions and geodynamics of the Baikal region, central Asia, Part 2. Cenozoic rifting, *Tectonophysics*, 282(1), 1–38
- Déverchère, J., Yelles, K., Domzig, A., Mercier de Lépinay, P., Bouillin, J-P., Gaullier, V., Bracène, R., Calais, E., Savoye, B., Kherroubi, K., 2 Le Roy, P., Pauc, H., & Dan, G. (2005). Active thrust faulting offshore Boumerdes, Algeria, and its relations to the 2003 Mw 6.9 earthquake. *Geophysical Research Letters* 32, L04311. <https://doi.org/10.1029/2004GL021646>
- Dewey, J.F., Helman, M.L., Turco, E., Hutton, D.H.W., & Knott, S.D. (1989). Kinematics of the Western Mediterranean. In *Alpine Tectonics*, 265–283, eds Coward, M.P., Dietrich, D. & Park, R.G., Geol. Soc. Spec. Publ.45, London.
- Domzig, A. (2006). Déformation active et récente, et structuration tectonosédimentaire de la marge sous-marine algérienne, Thèse de Doctorat. dissertation, 333 pp., Inst. Univ. Eur. de la Mer, Brest Univ., Brittany, France.
- Durand-Delga, M. (1969). Mise au point sur la structure du Nord-Est de la Berbérie. *Publ Serv Géol Algérie N° 39*:89–131
- Duverger, C., Godano, M., Bernard, P., Lyon-Caen, H., & Lambotte, S. (2015). The 2003–2004 seismic swarm in the western Corinth rift: Evidence for a multiscale pore pressure diffusion process along a permeable fault system. *Geophysical Research Letters*, 42, 7374–7382. <https://doi.org/10.1002/2015GL065298>
- Efron, B. (1982). The Jackknife, the Bootstrap and Other Resampling Plans. CBMS-NSF Regional Conference Series in Applied Mathematics, Monograph 38, SIAM, Philadelphia.
- Fossen, H. (2020). Fault classification, fault growth and displacement, *Regional Geology and Tectonics: Principles of Geologic Analysis*, pp. 119–147.
- Fossen, H., & Cavalcante, G. C. G. (2017). Shear zones—A review. *Earth-Science Reviews*, 171, 434–455. <https://doi.org/10.1016/j.earscirev.2017.05.002>
- Fossen, H., Johansen, S. E., Hesthammer, J., & Rotevatn, A. (2005). Fault interaction in porous sandstone and implications for reservoir management; examples from southern Utah. *American Association of Petroleum Geologists Bulletin*, 89, 1593–1606.
- Glaçon, J. (1967). Recherches sur la géologie et les gîtes métallifères du Tell sétifien. *Bulletin du Service Géologique de l'Algérie*, 552 p.
- Gospodinov, D., & Rotondi, R. (2006). Statistical Analysis of Triggered Seismicity in the Kresna Region of SW Bulgaria (1904) and the Umbria-Marche Region of Central Italy (1997). *Pure application geophys.* 163, 1597–1615. <https://doi.org/10.1007/s00024-006-0084-4>
- Guiraud, R. (1977). Sur la neotectonique des régions ouest-constantinoises. *Bulletin de la Société Géologique de France S7-XIX*:645–650. <https://doi.org/10.2113/gssgfbull.S7-XIX.3.645>
- Harbi, A., Maouche, S., & Ayadi, A. (1999). Neotectonics and associate seismicity in the Eastern Tellian Atlas of Algeria. *Journal of Seismology*, 3, 95–104.
- Harbi, A., Maouch, S., & Benhallou, H. (2003). Re-appraisal of seismicity and seismotectonics in the north-eastern Algeria Part II: 20th century seismicity and seismotectonics analysis. *Journal of Seismology*, 7, 221–234.
- Jackson, J. (1992). Partitioning of strike-slip and convergent motion between Eurasia and Arabia in eastern Turkey and the Caucasus. *JGR*, 97(B9), 12471–12479. <https://doi.org/10.1029/92JB00944>
- Jackson, J., Norris, R., & Youngson, J. (1996). The structural evolution of active fault and fold systems in central Otago, New Zealand: Evidence revealed by drainage patterns. *Journal of Structural Geology*, 18, 217–234.
- Jin, K., & Kim, Y. (2020). Importance of surface ruptures and fault damage zones in earthquake hazard assessment: A review and new suggestions. *Geological Society, London, Special Publications*, 501, 205–224. <https://doi.org/10.1144/SP501-2019-98>
- Kherroubi, A., Déverchère, J., Yelles, A. K., Mercier de Lépinay, B., Domzig, A., Cattaneo, A., Bracene, R., Gaullier, V., & Graindorge, D. (2009). Recent and active deformation pattern off the easternmost Algerian margin, western Mediterranean Sea: New evidence for contractional tectonic reactivation. *Marine Geology*, 261(1–4), 17–32. <https://doi.org/10.1016/j.margeo.2008.05.016>

- Kim, Y.-S., Andrews, J. R., & Sanderson, D. J. (2001). Reactivated strike-slip faults: Examples from north Cornwall, UK. *Tectonophysics*, *340*, 173–194.
- Kim, Y.-S., Peacock, D. C. P., & Sanderson, D. J. (2004). Fault damage zones. *Journal of Structural Geology*, *26*, 503–517.
- Kirèche, O. (1993). Evolution géodynamique de la marge tellienne des maghrebides d'après l'étude du domaine parautochtone schistose
- Kissling, E., Ellsworth, W. L., Eberhart-Phillips, D., & Kradolfer, U. (1994). Initial reference model in local earthquake tomography. *Journal of Geophysical Research*, *99*, 19635–19646.
- Klein, F. (2002). User's guide to HYPOINVERSE-2000, a Fortran program to solve for earthquake locations and magnitudes, USGS Open-File Report 02–171, vers. 1, p 123.
- Klingelhoefer, F., Déverchère, J., Graindorge, D., Aïdi, C., Badji, R., Bouyahiaoui, B., Leprêtre, A., Mihoubi, A., Beslier, M. O., Charvise, P., Schnurl, P., Sage, F., Medaouri, M., Arab, M., Bracene, R., Yelles-Chauouche, A. K., Badsî, M., Galvé, A., & Géli, L. (2022). Formation, segmentation and deep crustal structure variations along the Algerian margin from the SPIRAL seismic experiment. *Journal of African Earth Sciences*, *186*, 104433. <https://doi.org/10.1016/j.jafrearsci.2021.104433>
- Kohketsu, K. (1985). The extended reflectivity method for synthetic near field seismograms. *Journal of Physics of the Earth*, *33*, 121–131.
- Lin, J., & Stein, R. S. (2004). Stress triggering in thrust and subduction earthquakes, and stress interaction between the southern San Andreas and nearby thrust and strike-slip faults. *Journal of Geophysical Research*, *109*, B02303. <https://doi.org/10.1029/2003JB002607>
- Marre, A. (1992). Le Tell oriental algérien de Collo à la frontière tunisienne: Etude géomorphologique. O.P.U Alger, Volume II, Pages 413 à 624.
- Mauffret, A., Frizon de Lamotte, F., Lallemand, S., Gorini, C., & Maillard, A. (2004). E-W opening of the Algerian Basin (Western Mediterranean). *Terra Nova*, *16*, 257–264. <https://doi.org/10.1111/j.1365-3121.2004.00559.x>
- McGrath, A. G., & Davison, I. (1995). Damage zone geometry around fault tips. *Journal of Structural Geology*, *17*, 1011–1024.
- Meghraoui, M. (1988). Géologie des zones sismiques du nord de l'Algérie (paléosismologie, Tectonique active et synthèse sismotectonique). Thèse de Doctorat, université de Paris sud, Orsay, France
- Meghraoui, M., & Pondrelli, S. (2012). Active faulting and transpression tectonics along the plate boundary in North Africa. *Annals of Geophysics*, *55*(5), 2012. <https://doi.org/10.4401/ag-4970>
- Mihoubi, A., Schnürle, P., Benaïssa, Z., Badsî, M., Bracene, R., Djelil, H., Géli, L., Sage, F., Agoudjil, A., Klingelhoefer, F., Schnurle, P., & Benaïssa, Z. (2014). Seismic imaging of the eastern Algerian margin off Jijel: Integrating wide-angle seismic modeling and multichannel seismic pre-stack depth migration. *Geophysical Journal International*, *198*, 1486–1503. <https://doi.org/10.1093/gji/ggu179>
- Obert, D. (1981). Etude géologique des Babors orientaux (domaine tellien, Algérie). Thèse de Doctorat d'Etat, Université de Paris-VI, Mèm. Sc. Terre 81–32, 635 pp.
- Ogata, Y. (1988). Statistical models for earthquake occurrences and residual analysis for point processes. *Journal of American Statistical Association*, *83*(401), 9–27. <https://doi.org/10.1080/01621459.1988.1047856>
- Ogata, Y. (1998). Space-time point process models for earthquakes occurrences. *Annals of the Institute of Statistical Mathematics*, *50*, 379–402.
- Poli, M. E., & Renner, G. (2004). Normal focal mechanisms in the Julian Alps and Prealps: Seismotectonic implications for the Italian-Slovenian border region. *Bollettino Di Geofisica Teorica ed Applicata*, *45*(1–2), 51–69.
- Raoult, J.F. (1974). Géologie Du Centre De La Chaîne Numidique : Nord Du Constantinois, Algérie. Mémoires de la Société géologique de France, 162 p.
- Reuther, C.-D., Ben-Avraham, Grasso, M. (1993). Origin and role of major strike-slip transfers during plate collision in the central Mediterranean. *Terra Nova*, *5*, 249–257
- Robin, C. (1970). Etude géodynamique du massif volcanique de Cap Cavallo. Thèse de 3^e me Cycle Uni. P. et M. Curie, Paris VI, 130 pp
- Rothé, J.P. (1950). Les séismes de Kherrata et la sismicité de l'Algérie. Publ Serv Cartes Geol Algérie 4^e série
- Riedel, W. (1929). Zur mechanik geologischer brucherscheinungen. *Centralblatt Fur Mineralogie, Geologie, Und Paleontologie*, *1929B*, 354.
- Rivera, L., & Cisternas, A. (1990). Stress tensor and fault plane solutions for a population of earthquakes. *Bulletin of the Seismological Society of America*, *80*(3), 600–614.
- Schettino, A., & Turco, E. (2006). Plate kinematics of the Western Mediterranean region during the Oligocene and Early Miocene. *Geophysical Journal International*, *166*, 1398–1423. <https://doi.org/10.1111/j.1365-246X.2006.02997.x>
- Soumaya, A., Ben-Ayed, N., Rajabi, M., Meghraoui, M., et al. (2018). Active faulting geometry and stress pattern near complex strike-slip systems along the Maghreb region: Constraints on active convergence in the western Mediterranean. *Tectonics*, *37*, 3148–3173
- Strzeczynski, P., Déverchère, J., Cattaneo, A., Domzig, A., Yelles, K., Mercier de Lépinay, B., Babonneau, N., & Boudiaf, A. (2010). Tectonic inheritance and Pliocene-Pleistocene inversion of the Algerian margin around Algiers: Insights from multibeam and seismic reflection data. *Tectonics* <https://doi.org/10.1029/2009TC002547>
- Sylvester, A. G. (1988). Strike-slip faults. *Geological Society of America Bulletin*, *100*, 1666–1703.
- Talebian, M., & Jackson, J. (2002). Offset on the Main Recent Fault of NW Iran and Implication for the Late Cenozoic Tectonics of the Arabia-Eurasia Collision Zone. *Geophysical Journal International*, *150*, 422–439. <https://doi.org/10.1046/j.1365-246X.2002.01711.x>
- Tingay, M., Morley, C., Hillis, R. R., & Meyer, J. J. (2010). Present-day stress orientation in Thailand's basins. *Journal of Structural Geology*, *32*, 235–248.
- Toda, S., Stein, R.S., Richards-Dinger, K., Bozkurt, S.B. (2005). Forecasting the evolution of seismicity in southern California: animations built on earthquake stress transfer. *J. Geophys. Res. Solid Earth* *110*. van Hinsbergen, D.J.J., Vissers, R.L.M.,
- Vila, J.M. (1980). La chaîne alpine d'Algérie Orientale et des confins algéro-tunisiens. Thèse de Doctorat, Université P. et M. Curie-Paris.
- Villemaire, C. (1988). Les amas sulfurés du massif miocène de El Aouana (Algérie)- I. Dynamisme de mise en place des roches volcaniques et implications métallogéniques. *Journal of African Earth Sciences*, *7*, 133–148. [https://doi.org/10.1016/0899-5362\(88\)90060-7](https://doi.org/10.1016/0899-5362(88)90060-7)

- Waldhauser, F., & Ellsworth, W. L. (2000). A double-difference earthquake location algorithm: Method and application to the northern Hayward fault. *Bulletin of the Seismological Society of America*, *90*, 1353–1368.
- Wesnowsky, S. (1988). Seismological and structural evolution of strike-slip faults. *Nature*, *335*, 340–343. <https://doi.org/10.1038/335340a0>
- Yagi, Y., & Nishimura, N. (2011). Moment tensor inversion of near-source seismograms. *Bulletin of International Institute of Seismology and Earthquake Engineering*, *45*, 133–138.
- Yale, D.P. (2003). Fault and stress magnitude controls on variations in the orientation of in situ stress. In: Ameen, M. (Ed.), *Fracture and in-situ stress characterization of hydrocarbon reservoirs*: Geological Society of London Special Publication, vol. 209, pp. 55–64.
- Yelles-Chaouche, A. K., Abacha, I., Boulahia, O., Aidi, C., Chami, A., Belheouane, A., Rahmani, S. T., & Roubeche, K. (2021). The 13 July 2019 Mw 5.0 Jijel Earthquake, northern Algeria: An indicator of active deformation along the eastern Algerian margin. *Journal of African Earth Sciences*. <https://doi.org/10.1016/j.jafrearsci.2021.104149>
- Yelles-Chaouche, A.K., Boudiaf, A., Djellit, H., & Bracene, R. (2006). La tectonique active de la région nord-algérienne. *C. R. Géosciences*. 1–14.
- Yelles-Chaouche, A. K., Roger, J., Deverchere, J., Bracene, R., Domzig, A., Hébert, H., & Kherroubi, A. (2009). The 1856 Tsunami of Djidjelli (Eastern Algeria): Seismotectonics, Modelling and Hazard Implications for the Algerian Coast. *Pure and Applied Geophysics*, *166*, 283–300. <https://doi.org/10.1007/s0002400804336>

(Received August 17, 2022, revised March 21, 2023, accepted March 26, 2023, Published online April 5, 2023)